Full length article

Global DIC approach guided by a cross-correlation based initial guess for HR-EBSD and on-axis HR-TKD

Clément Ernould[a,b], Benoît Beausir[a,b,*], Jean-Jacques Fundenberger[a,b], Vincent Taupin[a,b], Emmanuel Bouzy[a,b]

[a] *Université de Lorraine, CNRS, LEM3, F-57000, Metz, France*
[b] *Laboratory of Excellence on Design of Alloy Metals for Low-Mass Structures (DAMAS), University of Lorraine, 7 rue Félix Savart, Metz 57073, France*

ARTICLE INFO

ABSTRACT

Digital image correlation (DIC) techniques usually performed on deforming speckle patterns are applied here on electron diffraction patterns (EDP) in order to map disorientations with high angular resolution, as well as geometrically necessary dislocation densities and elastic strains. The proposed approach relies on a DIC analysis which is conducted independently from the microscope calibration. It registers EDP as a whole through a single and large region of interest whose relative deformation with respect to a reference EDP is described by a first-order homography. Subpixel registration is performed iteratively in the spatial domain using an inverse-compositional Gauss-Newton (IC-GN) algorithm which integrates the correction of the optical distortions. Its robustness against large orientation changes as well as its computational efficiency are improved by mean of an automated and path-independent initial guess which fairly captures the effects of large rotations on the EDP. Using successive Fourier-Mellin and Fourier transforms based cross-correlation techniques, the initial guess measures the in-plane rotation and translation between the reference and the target EDP, respectively. The performances of the technique are illustrated in markedly plastically deformed steels using two electron diffraction techniques in the scanning electron microscope. A 15% deformed interstitial free steel is investigated by means of electron backscattered diffraction (EBSD) while a quenched and tempered oxide dispersed strengthened steel subjected to martensitic transformation is characterized using a recently developed on-axis Transmission Kikuchi Diffraction (TKD) configuration.

1. Introduction

Orientation imaging microscopy (OIM) [1,2] is a valuable electron diffraction based technique for the characterization of the microstructure of crystalline materials in terms of phase and crystallographic orientation. Electron diffraction patterns (EDP) are most commonly acquired by reflection in a scanning electron microscope (SEM) using the electron backscattered diffraction (EBSD) technique. Since its lateral spatial resolution is limited to about 50 nm [3,4], new SEM-based techniques emerged in the current decade in response to the rising interest for nanomaterials. In 2012, Keller & Geiss [5] proposed the Transmission Kikuchi Diffraction (TKD) technique reusing the EBSD hardware. A thin foil is observed in transmission with a lateral spatial resolution down to 10 nanometres, opening a new field of applications reviewed in [6]. In 2016, Fundenberger et al. [7,8] proposed an improved on-axis configuration, where the scintillator is placed beneath the specimen,

perpendicularly to the beam. As compared to the conventional TKD, EDP are almost undistorted while a higher scattered electron intensity is captured, shortening acquisition time by a factor 20 [9,10].

EDP acquired with any of these techniques have been commonly indexed for most than 20 years using the Hough transform (HT) method [11] whose accuracy is typically about 0.5−1° [12]. In 2015, Chen et al. [13] proposed a dictionary approach. As its name implies, a dictionary of precomputed EDP is first generated such that the orientation space is uniformly sampled. These patterns are then compared to the experimental ones using the inner product as a similarity metric in order to determine orientation with an accuracy typically about 0.7° and up to 0.2° for a well calibrated system [12,14]. If it overpasses the conventional HT-based indexation (HTI) in terms of robustness against noise and accuracy, this approach is computationally much more demanding. To overcome this drawback, Hielscher et al. [15] proposed in 2018 a spherical harmonic transform based approach where the dictionary is replaced by a simulated master pattern which alone accounts for the entire Kikuchi sphere. Very recently, Lenthe et al. [16] improved the computational efficiency of the technique, such that orientations are determined at a speed close to the HT real time indexing with an accuracy up to almost 0.1° with refinement.

* Corresponding author at: Laboratoire d'Etude des Microstructures et de Mécanique des Matériaux (LEM3, UMR CNRS 7239), Université de Lorraine, 7 rue Félix Savart - 57070 METZ, France.

E-mail address: benoit.beausir@univ-lorraine.fr (B. Beausir).

From the above methods, grain internal disorientations can then be derived from the Euler's angles. The results still remain less accurate than those obtained from the high angular resolution EBSD (HR-EBSD) technique. After the first attempts on semi-conductors in the 90′s [17,18], this technique experienced an impressive expansion in the 2000′s under the impetus of Wilkinson et al. [19–21]. Further improvements were proposed, notably by Maurice et al. and Britton et al. [22–25]. The HR-EBSD technique measures lattice rotation and elastic strain with an accuracy up to 10^{-4} (0,006°) on single crystals such as GaN and SiGe [26] or silicon subjected to four-point bending [27]. It was also applied for the first time to "off-axis" TKD [28] in 2018 to map the strain field in the vicinity of a single dislocation in tungsten or more recently to "on-axis" TKD [29]. In the HR-EBSD method, at least four non-collinear regions of interest (ROI) are picked up across two high-resolution EDP (typically 1000 × 1000 pixels), one reference EDP and one target EDP. Pairs of ROI are then cross-correlated in order to measure their relative shift with subpixel accuracy by fitting the near-peak-region of the cross-correlation function with a Gaussian. Since the technique is insensitive to hydrostatic deformation, the deviatoric elastic gradient tensor $\widehat{F}^e$ associated with the measured displacement field is obtained by solving iteratively an overdetermined (20–200 ROI are considered in practice) and weighted system [21,23,27]. Given that the diffraction signal originates from the surface vicinity for both EBSD [20] and TKD [30], a plane-stress assumption [20,24] is commonly made to determine the actual elastic deformation gradient F^e from the deviatoric one $\widehat{F}^e$. As proven by Hardin et al. [31], the stress normal to the free surface remains negligible in the absence of stress field sources located near the surface or of large error on the specimen tilt.

During this last year, three independent works by Vermeij & Hoefenagels [32], Ruggles et al. [33] and Shi et al. [34] proposed a 'global' HR-EBSD approach. This method is an 'integrated' Digital Image Correlation (I-DIC) approach [32,34] that correlates EDP signal intensities by using a unique and large ROI. The relative deformation of the target ROI with respect to the reference ROI is accounted for by eight degrees of freedom, which are the components of $\widehat{F}^e$. The deformation gradient is computed iteratively by means of a forward-additive (FA) [32,34] or an inverse-compositional (IC) [33] Gauss-Newton (GN) algorithm in order to solve the non-linear DIC problem, i.e. the minimization of the quadratic difference of intensities between the reference and the warped target ROI. The 'global' approach shows competitive performance as well as numerous advantages as compared to the 'local' one [33,34]. Bias related to the number of ROI, their location or weights is avoided. The absence of ROI overlapping avoids redundant calculations resulting in similar [33] or even faster [34] analysis times. Remapping of the EDP [24,25] is included in the GN algorithm and the potential of cross-grain measurement using this technique (i.e. the reference and target EDP belong to different grains) was demonstrated very recently by Vermeij et al. [35] using simulated patterns. Note that global DIC techniques are also emerging regarding the 'local' HR-EBSD technique, for which a novel remapping technique based on demon registration was very recently proposed by Zhu et al. [36].

In the present work, we probe the potential transfer to electron microscopy of existing advanced DIC techniques developed for the measurement of surface displacements and strains from speckle patterns deposited on mechanical samples [37,38]. Although developed independently from the works on global HR-EBSD approaches mentioned above, our method employs the same tools, i.e. an IC-GN algorithm applied to a large and single ROI. Our method however brings three notable originalities that are presented below. First, relative deformations of the ROI are measured independently from the SEM calibration, which is not the case for other global "integrated" DIC approaches or for the local approach with remapping. Indeed, the relative deformation of the ROI are modelled here by a first-order homography, which is a shape function often met in photogrammetry to described 2D projective transformations. Second, the correction of optical distortions is included in the IC-GN algorithm. Third, the

IC-GN algorithm is aided by a fully automated initial guess. It fairly accounts for the effects of (possibly large) rotations by measuring the in-plane rotation and translation between disoriented EDP by means of successive Fourier-Mellin and Fourier transforms based cross-correlation (FMT-CC, FT-CC), respectively. In this manuscript, we first detail the DIC approach and explain our choices for the algorithms used. The performances of the technique are then illustrated on plastically deformed metals. First, we analyse a 15% strained interstitial free (IF) steel where EDP were obtained from standard EBSD. Second, we further assess our method by analysing a quenched and tempered oxide dispersed strengthened (ODS) steel where transmission EDP were acquired by a recent on-axis TKD setup. For these plastically deformed materials, grain internal disorientation and geometrically necessary dislocation (GND) density maps are calculated. Our method is shown to work well for both EBSD and TKD diffraction patterns and allows analysing fine grain microstructures. Further, despite the medium resolution and the reduced signal-to-noise ratio of the EDP as compared to HR-EBSD standards, the method captures very fine details in the microstructure such as single dislocations or dislocation networks forming low-angle subgrain boundaries, which a standard HT-based indexation completely misses.

2. Global DIC approach

This section introduces an alternative 'uncoupled' approach that differentiates itself from the recently proposed global I-DIC approaches [32–34] in terms of both the initial guess (IG) and the subpixel registration (SR):

(i) The DIC analysis is independent from the SEM calibration. Relative deformations of the ROI are described by a first-order (linear) homography. The calibration parameters as well as their variation are considered afterwards to analytically deduce the deviatoric deformation gradient tensor. This results in a simple implementation of the algorithm and a separation of the DIC error from the uncertainty on calibration parameters.

(ii) Correction of the optical distortion of EDP is integrated into the IC-GN algorithm without substantially altering its numerical cost.

(iii) Subpixel registration is aided by a fully automated and path independent initial guess inspired from the one proposed by Pan et al. [39] for speckles patterns. Composed of successive FMT-CC and FT-CC analyses, this CC-based method ensures that the IC-GN algorithm converges despite the presence of rotation discontinuities such as at subgrain boundaries.

In addition to detailing the method, whose main steps are summed up in Fig. 1, this section also outlines the reasoning leading to the choice of the algorithms used.

1) DIC analysis

Initial guess

FMT-CC: estimation of the in-plane rotation

FT-CC: estimation of the remaining translation

Subpixel registration

IC-GN algorithm accounting for optical distortion

2) Solution computation

Accounting for the variations of the calibration parameters (correction of the homography)

Deducing the elastic deformation gradient

Polar decomposition (optional)

Fig. 1. Overview of the proposed method.

Fig. 2. Sketch illustrating the considered frame $\Re = O\left(\vec{X}_1, \vec{X}_2, \vec{X}_3\right)$, the scintillator and an ROI of size $\mathbf{M} \times \mathbf{N}$ pixels for which the centre is located at $\vec{x}_0$ with respect to the pattern centre (PC). $\vec{x}$ and $\vec{\xi}$ give the coordinates of a point in the ROI with respect to the PC or its centre, respectively.

In the following, an orthonormal frame $\Re = O(\vec{X}_1, \vec{X}_2, \vec{X}_3)$ attached to the diffraction volume is considered. $\vec{X}_3$ is perpendicular to the scintillator while $\vec{X}_1$ and $\vec{X}_2$ are aligned with the screen width and height, respectively (Fig. 2). *DD* refers to the sample to detector distance and *PC* denotes the pattern centre of the reference pattern. On the scintillator, the vector $X = \begin{pmatrix} x_1 & x_2 \end{pmatrix}^T$ gives the location with respect to the *PC* and $X_0 = \begin{pmatrix} x_{01} & x_{02} \end{pmatrix}^T$ is the geometric centre of a ROI of size $M \times N$ pixels. For points belonging to the ROI, ξ indicates their position with respect to its centre, i.e. $\boldsymbol{\xi} = X - X_0$. Let $r(\xi)$ and $t(\xi)$ be the functions describing the intensity within the reference ('*REF*') and target ('*TGT*') ROI, with mean value $\bar{r}$ and $\bar{t}$, respectively, such that one can define $\tilde{r}(\boldsymbol{\xi}) = r(\boldsymbol{\xi}) - \bar{r}$ and $\tilde{t}(\boldsymbol{\xi}) = t(\boldsymbol{\xi}) - \bar{t}$.

2.1. 'uncoupled' DIC based on a homography

Image registration methods are either area-based or feature-based. The second are acknowledged to encounter fewer limitations [40] and should be preferred when images contain sufficient distinctive and easily detectable objects. EDP contain many salient features such as line intersections which are suitable for an automated detection. The numerous symmetries in EDP however make their distinction questionable. On the other side, none of the major limitations of area-based methods [40] listed hereafter is nowadays prohibitive anymore. (i) The requirement of 'remarkable' content of the ROI is fulfilled, as it has already been proven by the local HR-EBSD technique. (ii) The increasing available computing power and the recent progress in DIC algorithms enable complex deformations of the ROI to be accounted for, which is paramount to avoid loss of accuracy [40,37,38]. (iii) Pattern filtering and the use of robust correlation criterions reduce the sensitivity of the similarity degree between two ROI to intensity changes such as noise or varying illumination.

An area-based approach is consequently developed. The zero-mean normalised cross-correlation criterion C_{ZNCC} (Eq. (1)) and the zero-mean normalized sum of squared difference criterion C_{ZNSSD} (Eq. (2)) are adopted for the initial guess and subpixel registration, respectively. These are different but related criterions [41] which offer the most robust noise-proof performance while being insensitive to linear brightness variations [40].

$$C_{ZNCC} = \sum_{\xi} \left[\frac{\tilde{r}(\boldsymbol{\xi}).\tilde{t}(\boldsymbol{\xi})}{\Delta\tilde{r}.\Delta\tilde{t}} \right] \quad where \quad \Delta\tilde{r} = \sqrt{\sum_{\xi} \tilde{r}(\boldsymbol{\xi})^2} \quad and \quad \Delta\tilde{t} = \sqrt{\sum_{\xi} \tilde{t}(\boldsymbol{\xi})^2}$$

(1)

$$C_{ZNSSD} = \sum_{\xi} \left[\frac{\tilde{r}(\boldsymbol{\xi})}{\Delta\tilde{r}} - \frac{\tilde{t}(\boldsymbol{\xi})}{\Delta\tilde{t}} \right]^2$$

(2)

Recovering lattice rotation and elastic strain implies to catch their effect on the scintillator with subpixel accuracy [21]. Since the

displacement field across EDP is assumed to be continuous, it can potentially be described by a parametric model known as the shape (or warp) function $W(\boldsymbol{p})$ where $\boldsymbol{p}$ is the vector containing the deformation parameters. The matrix $W(\boldsymbol{p})$ operates on each location ξ within the (undeformed) reference subset, such that the matching position ξ' within the (deformed) target subset can be expressed as:

$$\boldsymbol{\xi'} = W(\boldsymbol{p}).\boldsymbol{\xi}.$$

(3)

Depending on the number of parameters and their arrangement, displacements as well as displacement gradients can be modelled in a linear or more complex way. Following recommendations in [37,38], the ROI has to be taken as large as possible providing the shape function reasonably fits the underlying displacement field. If it is unfortunately not possible, this area can be divided into smaller regions where the displacement field is simpler, as it is done in the local HR-EBSD technique.

The first-order homography is composed of 8 deformation parameters h_{ij} stored in $\boldsymbol{p}$ as follows:

$$\boldsymbol{p} = \begin{pmatrix} h_{11} & h_{12} & h_{13} & h_{21} & h_{22} & h_{23} & h_{31} & h_{32} \end{pmatrix}^T$$

(4)

and a usual parametrization [42,43] is given by:

$$W(\boldsymbol{p}) = \begin{pmatrix} 1+h_{11} & h_{12} & h_{13} \\ h_{21} & 1+h_{22} & h_{32} \\ h_{31} & h_{32} & 1 \end{pmatrix}.$$

(5)

Fig. 3 illustrates the effect of each deformation parameter. The resemblance with transformations observed on the scintillator is striking.

In the following, we consider 'homogenous coordinates' (HC) which are often preferred to Euclidian coordinates (EC). Indeed, projective transformations can then be described by a matrix like in Eq. (5) and all points are represented with finite coordinates, even those at infinity. The qualifier 'homogenous' originates from the homogeneous property:

$$\forall \lambda \in \mathbb{R}^*, \ \boldsymbol{\xi} = \lambda.\boldsymbol{\xi}$$

(6)

Given a point on the scintillator $\boldsymbol{\xi} = \begin{pmatrix} \xi_1 & \xi_2 \end{pmatrix}^T$ in EC, it admits an infinity of possible representations by means of a three-dimensional vector $\boldsymbol{\xi} = \begin{pmatrix} u & v & w \end{pmatrix}^T$ in HC provided that $u^2 + v^2 + w^2 \neq 0$. Let us assume that w is non-zero. One can thus perform computations in HC and then simply divide the components of ξ by w according to the 'homogeneous property' to get back to EC (i.e. $\xi_1 = u/w$ and $\xi_2 = v/w$). In other words, when the last component is 1 in HC, the others correspond to the Euclidian coordinates. $\boldsymbol{\xi} = \begin{pmatrix} \xi_1 & \xi_2 & 1 \end{pmatrix}^T$ is consequently chosen as a

Fig. 3. Effect of each deformation parameter composing the first-order homography (Eq. (5)).

convenient representation during the DIC analysis, where ξ_1 and ξ_2 are calculated from the absolute location in EC of X and X_0 within the EDP. Knowing the pattern centre location (i.e. x_{01} and x_{02}) is thus not required at this stage. Eqs. (3) and (5) lead to

$$
\begin{pmatrix} \xi_1' \\ \xi_2' \\ 1 \end{pmatrix} = \begin{pmatrix} \dfrac{(1+h_{11}).\xi_1 + h_{12}.\xi_2 + h_{13}}{h_{31}.\xi_1 + h_{32}.\xi_2 + 1} \\ \dfrac{h_{21}.\xi_1 + (1+h_{22}).\xi_2 + h_{23}}{h_{31}.\xi_1 + h_{32}.\xi_2 + 1} \\ 1 \end{pmatrix} \tag{7}
$$

after dividing all components by the third one. The latter is reasonably assumed to be non-zero as the homography is not likely to be degenerated [42] (i.e. the warped target ROI is not reduced to a line).

At the end of the DIC analysis, all deformation parameters of the homography are obtained. The SEM calibration is then considered in order to interpret them in terms of lattice rotations and elastic strains. First, the deformation parameters h_{ij} are corrected to account for the variation of the projection geometry. The PC displacement is responsible for a uniform translation by a vector $(\Delta_1^{PC} \quad \Delta_2^{PC})^T$ of the target EDP with respect to the reference. Variations of DD also generate an isotropic scaling by a factor $\alpha = DD^{TGT}/DD^{REF}$ with respect to the pattern centre of the target EDP. As shown on the Fig. 3 and detailed in the Appendix A, the DIC captures these effects (planar translations in h_{13} and h_{23}, scaling in both h_{11} and h_{22}) so that the corrected parameters $\hat{h}_{ij}$ are deduced from the measured ones h_{ij} as follows:

$$
\begin{pmatrix} \hat{h}_{11} & \hat{h}_{12} & \hat{h}_{13} \\ \hat{h}_{21} & \hat{h}_{22} & \hat{h}_{23} \\ \hat{h}_{31} & \hat{h}_{32} & 1 \end{pmatrix}
$$
$$
= \begin{pmatrix} \dfrac{h_{11}+1-\gamma_1.h_{31}}{\alpha}-1 & \dfrac{h_{12}-\gamma_1.h_{32}}{\alpha} & \dfrac{h_{13}-\gamma_1}{\alpha} \\ \dfrac{h_{21}-\gamma_2.h_{31}}{\alpha} & \dfrac{h_{22}+1-\gamma_2.h_{32}}{\alpha}-1 & \dfrac{h_{23}-\gamma_2}{\alpha} \\ h_{31} & h_{32} & 1 \end{pmatrix} \tag{8}
$$

where $\quad \gamma_i = \alpha.\Delta_i^{PC} + x_{0i}.(\alpha-1)$

Eq. (7) is now rearranged in order to replace the homography in the context of the HR-EBSD problem,

$$
\begin{pmatrix} x_1' \\ x_2' \\ x_3' \end{pmatrix} = \begin{pmatrix} \dfrac{DD.\left(\hat{F}_{11}^e.x_1+\hat{F}_{12}^e.x_2+\hat{F}_{13}^e.x_3\right)}{\hat{F}_{31}^e.x_1+\hat{F}_{32}^e.x_2+\hat{F}_{33}^e.x_3} \\ \dfrac{DD.\left(\hat{F}_{21}^e.x_1+\hat{F}_{22}^e.x_2+\hat{F}_{23}^e.x_3\right)}{\hat{F}_{31}^e.x_1+\hat{F}_{32}^e.x_2+\hat{F}_{33}^e.x_3} \\ x_3 \end{pmatrix} \tag{9}
$$

where $x_3 = x_3' = DD$ and $\hat{F}_{33}^e = 1$. To this end, its right side is multiplied by the sample-to-detector distance DD using the homogeneous property while ξ is expressed as a function of the pattern centre (i.e. x_{01} and x_{02}). Detailed calculations are available in Appendix B. Term-by-term identification of the so-rearranged Eq. (7) with Eq. (9) analytically gives $\hat{F}^e$:

$$
\begin{pmatrix} \hat{F}_{11}^e & \hat{F}_{12}^e & \hat{F}_{13}^e \\ \hat{F}_{21}^e & \hat{F}_{22}^e & \hat{F}_{23}^e \\ \hat{F}_{31}^e & \hat{F}_{32}^e & 1 \end{pmatrix} =
$$

$$
\begin{pmatrix} \dfrac{1+\hat{h}_{11}+\hat{h}_{31}.x_{01}}{1-\hat{h}_{31}.x_{01}-\hat{h}_{32}.x_{02}} & \dfrac{1+\hat{h}_{12}+\hat{h}_{32}.x_{01}}{1-\hat{h}_{31}.x_{01}-\hat{h}_{32}.x_{02}} & \dfrac{\hat{h}_{13}-\hat{h}_{11}.x_{01}-\hat{h}_{12}.x_{02}-\hat{h}_{32}.x_{01}.x_{02}-\hat{h}_{31}.x_{01}^2}{DD.\left(1-\hat{h}_{31}.x_{01}-\hat{h}_{32}.x_{02}\right)} \\ \dfrac{1+\hat{h}_{21}+\hat{h}_{31}.x_{02}}{1-\hat{h}_{31}.x_{01}-\hat{h}_{32}.x_{02}} & \dfrac{1+\hat{h}_{22}+\hat{h}_{32}.x_{02}}{1-\hat{h}_{31}.x_{01}-\hat{h}_{32}.x_{02}} & \dfrac{\hat{h}_{23}-\hat{h}_{21}.x_{01}-\hat{h}_{22}.x_{02}-\hat{h}_{31}.x_{01}.x_{02}-\hat{h}_{32}.x_{02}^2}{DD.\left(1-\hat{h}_{31}.x_{01}-\hat{h}_{32}.x_{02}\right)} \\ \dfrac{DD.\hat{h}_{31}}{1-\hat{h}_{31}.x_{01}-\hat{h}_{32}.x_{02}} & \dfrac{DD.\hat{h}_{32}}{1-\hat{h}_{31}.x_{01}-\hat{h}_{32}.x_{02}} & 1 \end{pmatrix}. \tag{10}
$$

As a consequence:

(i) A first-order homography is perfectly suitable for the HR-EBSD problem as it does not under-match nor over-match the deformation occurring between the reference and the target EDP.

(ii) A single ROI is consequently necessary and sufficient. Ideally, it should be taken as large as possible [37,38] such that the DIC analysis will consider the EDP as a whole through a unique and large ROI.

(iii) The $\hat{F}_{ij}^e$ components are deduced analytically from the corrected $\hat{h}_{ij}$ parameters and vice-versa (see Eq. (14) in the next section).

If the shape function describes the displacement field, its measurement is the aim of the Lucas-Kanade optical flow algorithm [44]. Accounting for relative deformation however produces non-linearity of the sum of squared difference criterion, whose minimization becomes computationally intensive. Fortunately, surface displacement and deformation measurement by DIC has experienced during the last decade tremendous improvements that are reviewed in [37,38]. The Lucas-Kanade method is now applied through computationally efficient iterative spatial cross-correlation algorithms with subpixel accuracy. The most commonly used are the forward additive Newton-Raphson (FA-NR) algorithm introduced by Bruck et al. [47], the forward additive Gauss-Newton (FA-GN) and the inverse compositional Gauss-Newton (IC-GN) algorithm proposed by Baker & Matthews [45,46].

Providing that the shape function W is differentiable with respect to p, such algorithms compute the increment Δp of the deformation vector p at each iteration until a convergence criterion is fulfilled or a maximal number of iterations is reached. As their name implies, these algorithms differentiate themselves through their optimization algorithm and through the manner p is updated, using either a forward additive scheme

$$p = p + \Delta p \tag{11}$$

or an inverse compositional scheme

$$W(p) = W(p) \circ W^{-1}(\Delta p). \tag{12}$$

For the second scheme, the shape function W has also to be invertible.

The IC-GN algorithm has been adopted here because it is up to 5 times faster than the FA-NR algorithm [48] while showing better noise-proof performance with similar accuracy [49]. It has also the same level of accuracy than the FA-GN algorithm and considering a homography, Baker & Matthews [43] showed that both algorithms converge at the same rate. However, the reference ROI remains unchanged along iterations with the inverse-compositional scheme, resulting in a significant drop of the calculation effort. Indeed, the GN—Hessian matrix (see [43]) remains unchanged for a given reference since it is computed for $p = 0$.

2.2. Correction of the optical distortion

Although EBSD detectors aim at minimizing optical distortion, a correction is required for accurate strain measurements [45]. Such correction is integrated into the IC-GN algorithm by considering the corrected locations $\hat{\xi} = \hat{X} - \hat{X}_0$ indicated by the red dots in Fig. 4a instead of the initial regular grid (black dotted lines). The images of these points by the homography directly gives the corrected coordinates $\hat{\xi}'$ to interpolate within the (distorted) target pattern (red dots in Fig. 4b). The computational cost of the DIC analysis remains (quasi) unchanged. Assuming that the optical distortion is identical for all EDP, the corrected $\hat{\xi}$ are precomputed only once. As compared to a regular grid where each ξ is located on

(a) Reference ROI   (b) Warped target
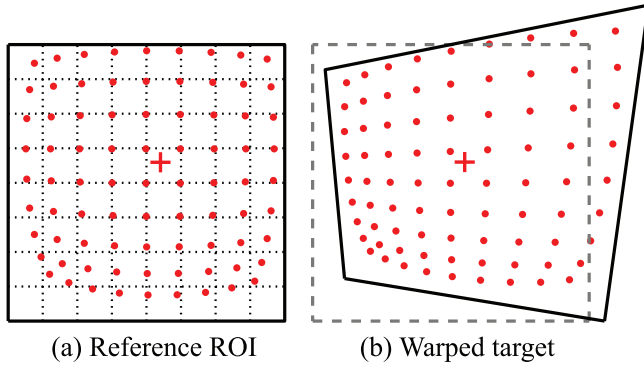
Fig. 4. Scheme illustrating the relative deformations between the reference ROI (a) and the warped target ROI (b) under a homography in the absence of optical distortion (ROI edges in black). The red cross indicates the optical centre while the red dots are the corrected locations to interpolate within the optically distorted patterns. Note that radial and tangential distortion effects are exaggerated here. (For interpretation of the references to colour in this figure legend, the reader is referred to the web version of this article.)

integer pixel (dotted lines in Fig. 4a), such a correction will only result in additional interpolations of the reference image and its gradients during the computation of the GN—Hessian matrix (red spots in Fig. 4a). Note that its cost is already negligible thanks to the inverse-compositional scheme.

2.3. A fully automated and cross-correlation based initial guess

The GN algorithm converges to a local extremum and should therefore be initialised with a vector of deformation parameters p_0 sufficiently close to the solution. The accuracy of the initial guess directly affects the convergence characteristics of both FA-GN and IC-GN algorithms [38]. As illustrated in the context of HR-EBSD by Vermeij and Hoefnagels [32] and Ruggles et al. [33] by using dynamically simulated patterns, the convergence speed decreases with increasing disorientation between the initial guess and the true solution. Divergence is likely to occur for differences over $\sim 1°$, which is of the order of the Hough-transform based indexation uncertainty. Besides accuracy concerns, different strategies exist to provide an initial guess [38]. The algorithm can be initialized at one point in the orientation map from the solution at neighbouring points. Such an approach is however path dependant and it is expected to fail in the presence of rotation discontinuities like at subgrain boundaries. It should also be reliability-guided to avoid error propagation [46]. Path independent approaches circumvent these limitations.

From this standpoint, a self-contained and path independent method proposed by Pan et al. [47] for correlating speckle patterns that differ by a scale, a translation and an in-plane rotation up to $\pm 180°$ is transferred here to electron microscopy. It pre-aligns images in a fully automated way. Its working principle is based on the four following steps:

1. Measurement of the in-plane rotation θ_3 (around $\vec{X_3}$) by mean of a Fourier-Mellin transform based cross-correlation (FMT-CC).
2. Rotation of the reference ROI around its centre by θ_3.
3. Measurement of the remaining planar translation $\vec{\Delta} = \Delta x_1 \vec{X_1} + \Delta x_2 \vec{X_2}$ by mean of a Fourier transform-based cross-correlation (FT-CC).
4. Initialisation of the eight deformation parameters of the homography according to ($\theta_3, \Delta x_1, \Delta x_2$).

Note that the method has been adapted to the specificities of electron microscopy. The implementation of the first three steps is detailed and illustrated in the Appendix C. As highlighted for both on-axis TKD and EBSD patterns in Fig. 5, the method fairly accounts

for the effect of disorientation. It applies similarly for both EBSD and on-axis TKD techniques, except the additional use of a mask with noise on the reference pattern in the case of on-axis TKD (Fig. 5a (top)) in order to remove the transmitted beam and diffraction spots. Otherwise the latter would act as anchors, leading to an erroneous measurement of the translation (see Appendix C).

The homography is initialized from the measured rotation and translation. Pan et al. [47] consider a first-order affine shape function whose deformation parameters corresponds to the six first parameters of the homography. Following [47], the initialization is taken here as

$$p_0 = \begin{pmatrix} \cos(\theta_3) - 1 & -\sin(\theta_3) & \Delta x_1 & \sin(\theta_3) & \cos(\theta_3) - 1 & \Delta x_2 & 0 & 0 \end{pmatrix}^T,$$

(13)

where the two additional parameters h_{31} and h_{32} of the homography are simply set to zero. The warped target ROI remains a square when using this 'partial' initialization (Fig. 5c). It may become problematic with increasing rotations, especially concerning EBSD patterns whose distortion is greater than those with the on-axis TKD configuration. A 'complete' initialization is also possible but requires an a priori knowledge of the SEM calibration. The accuracy of SEM calibration is not critical at this stage as the objective is to provide an initial guess. The rotation angles θ_1 and θ_2 can indeed be estimated from translation by taking the arc-tangent of $\Delta x_i / DD$ ($i = 1, 2$). In this case, a rotation matrix is then computed and provides an estimation of F^e. All the deformation parameters are finally initialised as follow:

$$\begin{pmatrix} h_{11} & h_{12} & h_{13} \\ h_{21} & h_{22} & h_{23} \\ h_{31} & h_{32} & 1 \end{pmatrix} = \frac{1}{DD + \widehat{F}_{31}.x_{01} + \widehat{F}_{32}.x_{02}} \begin{pmatrix} K_{11} & DD.\widehat{F}_{12}^e - \widehat{F}_{32}^e.x_{01} & K_{13} \\ DD.\widehat{F}_{21}^e - \widehat{F}_{31}^e.x_{02} & K_{22} & K_{23} \\ \widehat{F}_{31}^e & \widehat{F}_{32}^e & 1 \end{pmatrix}$$

(14)

Where

$$K_{11} = DD.\left(\widehat{F}_{11}^e - 1\right) - 2.\widehat{F}_{31}^e.x_{01} - \widehat{F}_{32}^e.x_{02}$$

$$K_{22} = DD.\left(\widehat{F}_{22}^e - 1\right) - \widehat{F}_{31}^e.x_{01} - 2.\widehat{F}_{32}^e.x_{02}$$

$$K_{13} = DD.\left[\left(\widehat{F}_{11}^e - 1\right).x_{01} + \widehat{F}_{12}^e.x_{02} + \widehat{F}_{13}^e.DD\right] - \widehat{F}_{31}^e .x_{01}^2 - \widehat{F}_{32}^e.x_{01}.x_{02}$$

$$K_{23} = DD.\left[\widehat{F}_{21}^e.x_{01} + \left(\widehat{F}_{22}^e - 1\right).x_{02} + \widehat{F}_{23}^e.DD\right] - \widehat{F}_{31}^e.x_{01}.x_{02} - \widehat{F}_{32}^e .x_{02}^2$$

where the $\widehat{F}_{ij}^e$ components are obtained by normalizing F^e by F_{33}^e. Indeed, Eq. (14) is the reciprocal of Eq. (10) where $\widehat{F}_{33}^e = 1$. Note that it can be used more generally to initialize the homography from any estimation of the elastic deformation gradient tensor expressed in $\Re$, such as the one provided by the indexation for instance (i.e. F^e is a rotation matrix built from the disorientation between the target and the reference crystal).

3. Materials and methods

3.1. Specimens and data acquisition

Two plastically deformed materials are investigated using two different SEM-based techniques:

(i) A bulk specimen of IF steel subjected to a quasi-static uni-axial tensile test up to 15% strain, mechanically polished and observed using EBSD.

(ii) A thin foil of tempered 9Cr-ODS martensitic steel obtained by twin-jet electro polishing and characterized by means of on-axis TKD. The ODS sample is obtained by austenizing at 1050 °C for 10 min, quenching with helium gas and then, tempering at 600 °C for 20 mn followed by air cooling. Strong plastic shear deformations

| (a) Reference subset | (b) Target subset (unwarped) | (c) Pre-aligned target subset |
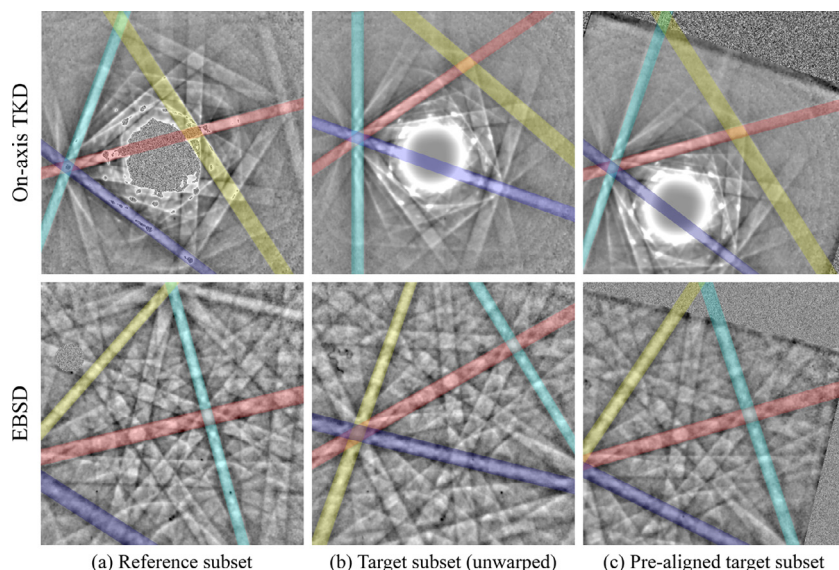
Fig. 5. Examples of image pre-alignment. (top) on-axis TKD patterns disoriented by $\sim 20°$ (bottom) EBSD patterns disoriented by $\sim 23°$ (a) Reference subset, with a mask applied in the case of TKD. (b) Target subset. (c) Warped target subset according to the initial guess.

are generated during the martensitic transformation. Then, partial recovery of strains and dislocation substructures occurs during the tempering treatment.

All presented data are acquired with a FEG-SEM Zeiss Supra 40 and Bruker's ESPRIT 1.9 software. The SEM is equipped with two Bruker e^- Flash HR+ cameras, one for EBSD and one associated to a Bruker OPTIMUS detector for on-axis TKD (both configurations are illustrated in Fig. 1 in [48]) for which a forescatter electron detector (FSD) composed of three diodes is also placed at the bottom of the scintillator. The obtained colour images provide qualitative information in a very sensitive way on crystal orientation, surface topography or phases [49] or even magnetic surface domains [50]. Table 1 sums up the acquisition parameters. In comparison with HR-EBSD standards, 16-bits grayscale patterns are recorded without background correction with a medium resolution of 600×600 px^2 using short exposure times. On the one hand, acquisition time is limited by beam drift considerations, especially regarding the ODS steel. On the other hand, plastic deformation mostly degrades the sharpness of the Kikuchi patterns which cannot be significantly improved by longer exposure times.

3.2. SEM calibration

SEM calibration is performed with the Bruker's ESPRIT 1.9 software for both EBSD and on-axis TKD datasets. It is based on the iterative pattern fitting method [51]. Despite the resolution of the Hough-transform is set to the maximum, this method is insufficient for accurate elastic strain measurement [22,45] since the pattern centre is located with an uncertainty typically the order of 0.5% of the image width. Although this is known to be responsible for phantom strains of the order of 10^{-3}, localizing the pattern centre with accuracy is still a challenging task that has not been achieved yet on such experimental cases, because of pattern blurring and the miss of any easily

| (a) Raw pattern | (b) Filtered pattern | (c) Mask applied |
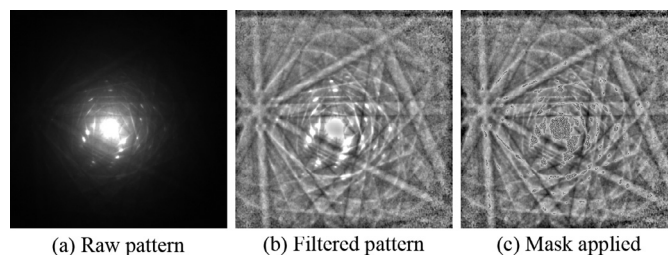
Fig. 6. (a) On-axis TKD pattern acquired in the ODS steel at the location indicated by a cross on Fig. 8a. (b) After filtering. (c) After applying a mask to hide the spots.

identifiable strain-free reference. Besides from the precise knowledge of the calibration parameters, their variation across the orientation map is also critical since neglecting them may lead to spurious strain components of the order of $\sim 4.10^{-3}$ [23,27,45]. These variations are thus estimated knowing the map step size and the SEM configuration. Finally, the optical distortions can also generate phantom strains having similar magnitudes [52]. Their effects are the most pronounced when moving away from the optical centre, i.e. near the edges of the EDP which are particularly noisy regions here due to the thermomechanical state of the investigated materials (Figs. 5 and 6). Because of this and the current limitations on the SEM calibration, the optical distortion correction option is not used in the following, especially since the values of the aberrations for the used detectors are unknown and not measured.

3.3. Data processing

The filtering of the raw EDP and the whole DIC analysis are programmed in Fortran and implemented in the ATEX-software [53] developed in our lab. The IC-GN algorithm is performed according to [54] such that the C_{ZNSSD} criterion (Eq. (2)) is minimised, EDP and

Table 1
SEM settings for data acquisition.

Material	Technique / Magnification	Voltage [kV]	Current [nA]	Working distance / Detector distance [mm]	Step size [nm]	Exposure [ms] / Frame averaging
IF steel	EBSD / x1600	20	7.1	15.26 / 16.29	220	75 / 2
ODS steel	on-axis TKD / x37k	30	1.25	3.75 / 24.63	10	40 / 1

their spatial gradients are interpolated considering biquintic B-splines, consistently with recommendations in [37,38]. All necessary equations are detailed in [54] except the convergence criterion and the Jacobian that are given in the Appendix D. According to common values from the literature [47,55,56], the convergence criterion of the IC-GN algorithm is set to 0.001 px. ROI of size 512 × 512 px^2 and 471 × 471 px^2 are extracted from the centre of the EDP for the initial guess and the subpixel registration, respectively.

As compared to EBSD and conventional TKD, on-axis TKD patterns display a much larger dynamics in the intensities (Fig. 6a) for which no dedicated treatment is yet proposed in the literature. In order to improve the EDP, a high-pass log filter (Appendix E) is applied for continuous background removal, followed by median and Gaussian filters with a radius of 1 pixel to reduce high-frequency noise. Intensities are then normalised (Fig. 6b). In the case of the reference pattern only, a mask with noise is also applied during the whole DIC in order to hide the transmitted beam and most of the diffraction spots. Such a mask is set by the intensities that exceed a threshold defined by the user.

4. Applications

This section illustrates the performances of the technique. Results will be discussed in terms of grain internal disorientations and geometrically necessary dislocation densities, which are of valuable interest for the understanding of deformation mechanisms and for strain gradient crystal plasticity modelling [57]. In most of crystalline materials, the emergence of disorientations in the course of plastic deformation is correlated with the formation of dislocations structures having a non-null net Burger's vector, such as dislocation pile-ups, cells or subgrain boundaries. The geometrically necessary dislocation densities relate lattice rotation gradients (curvatures) to such arrangements of dislocations and can be estimated according to the Nye-Kröner theory [58−60]. Because of the insufficient accuracy on SEM calibration (see section 3.2), elastic strains remain questionable and are consequently neglected in the calculation of the GND densities. This is a reasonable and usual assumption for the study of plastically deformed materials by means of HR-EBSD [61,62].

Computations are performed on a per-grain basis. A tolerance angle of 5° is used to define grain boundaries. For each grain, the reference pattern is automatically selected by determining the gravity centre of the grain and then by looking for the closest pattern having a band contrast which worth at least 90% of the maximum observed within the grain. DIC computations are performed in the scintillator frame $\Re$ but results are then expressed in the sample frame. The intra-granular disorientation at each point in a given grain is calculated with respect to the reference of the grain. The GND densities are then derived from the lattice curvature κ approximated with a finite difference scheme applied on the disorientations $\boldsymbol{\theta} = \begin{pmatrix} \theta_1 & \theta_2 & \theta_3 \end{pmatrix}^T$ as follows [60]:

$$\kappa_{ij} \cong \Delta\theta_i / \Delta x_j, \tag{15}$$

where Δx_j is the step size of the orientation map in the direction x_j. By neglecting the elastic strains, the Nye's dislocation tensor $\boldsymbol{\alpha}$ is then obtained by

$$\boldsymbol{\alpha} \cong tr(\boldsymbol{\kappa}).\boldsymbol{I} - \boldsymbol{\kappa}^T. \tag{16}$$

Its entrywise norm

$$\| \boldsymbol{\alpha} \| = \sqrt{\alpha_{ij} \cdot \alpha_{ij}} \tag{17}$$

will be displayed hereafter. Results are expressed in μm^{-1} but they can be converted in m^{-2} by dividing them by the magnitude of the burgers vector b. Here, if $b = 0.25$ nm, 1 μm^{-1} corresponds to 4×10^{15} m^{-2}.

4.1. EBSD: IF steel

Results for the IF steel are displayed on Fig. 7. Note that the EBSD patterns shown in Fig. 5 (bottom) are extracted from this dataset.

Black crosses indicate their location on Fig. 7a. For better colour visualisation purpose, disorientation angles ranging from 0 to 8° are plotted except within regions delimited by a black dash-line. In these regions, larger disorientations up to $\sim$ 12° are present and the scale is consequently adjusted. The disorientation map with the HTI (Fig. 7a) and the associated map of the Nye's tensor norm (Fig. 7b) should be compared to those obtained using the DIC analysis aided by the proposed CC-based IG in Fig. 7c and 7d, respectively. For a better comparison with the HTI, profiles of the disorientations and GND densities are presented in Fig. 9a and c, respectively. The disorientations calculated from the HTI are clearly noisy, far more than those from the DIC analysis. This noise leads inevitably to an erroneous estimation of the spatial derivatives involved in the GND density calculation. The DIC analysis reveals thus dislocation patterns and low-angle subgrain boundaries (Fig. 7d) that a standard HTI mostly misses (Fig. 7b). The latter boundaries are in agreement with the small orientation changes observed on the simulated FSD image (Fig. 7f). Such a coloured image is computed using the ATEX-software [53] by integrating the lower third of EDP with blue, green and red channels. Each one is catching intensities from the left, the middle or the right side of the pattern, respectively, just as real FSD diodes would do in practice.
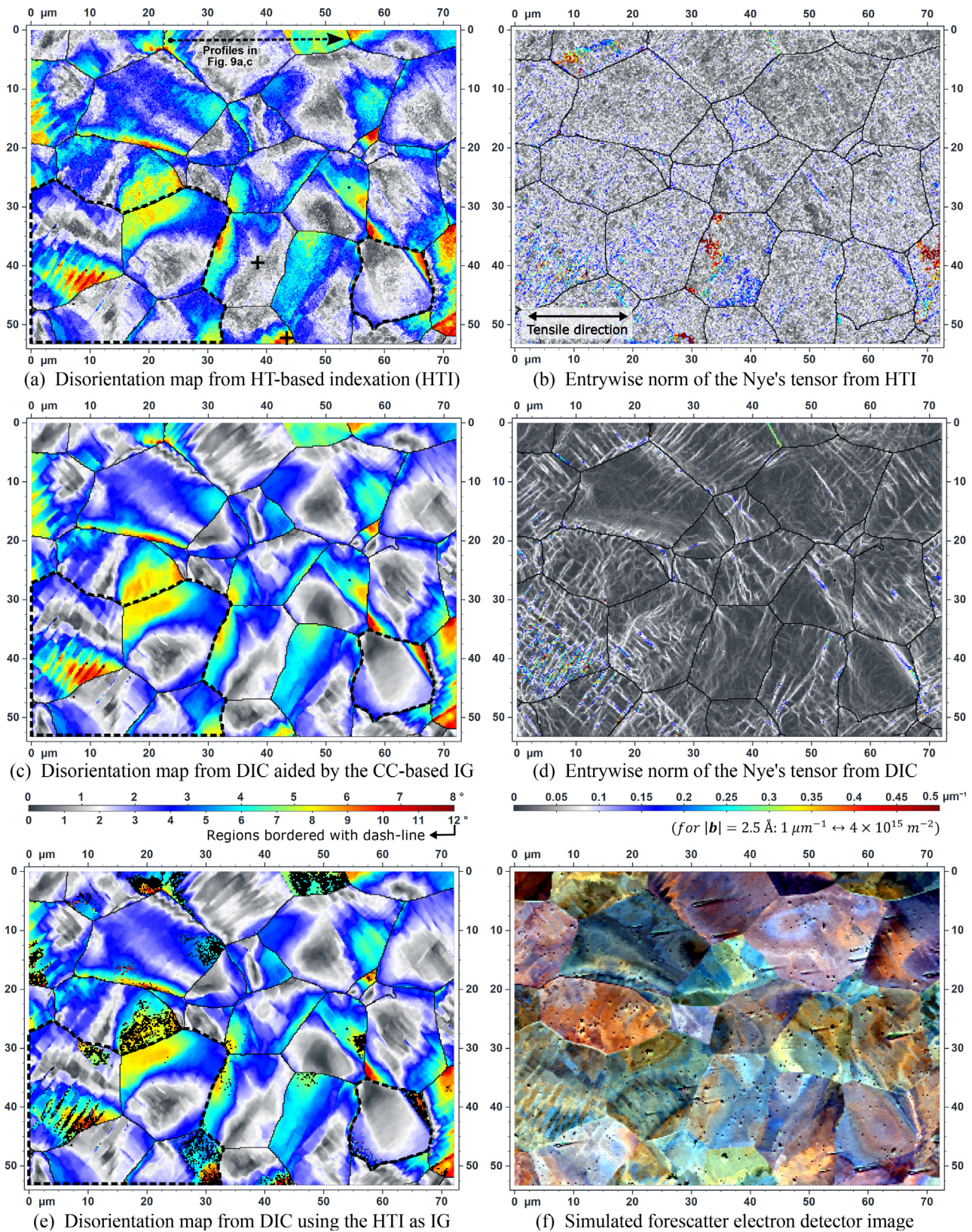
4.2. On-axis TKD: ODS steel

Fig. 8 shows the results obtained for the ODS steel by means of on-axis TKD, for which case a typical reference pattern is displayed in Fig. 6. The latter is one of the highest quality patterns amongst the dataset. As expected, the disorientation map deriving from the HTI (Fig. 8a) and the associated Nye's tensor norm (Fig. 8b) miss most of the microstructure details which are visible on the experimental FSD image shown in Fig. 8d. Indeed, only large structures such as the subgrain boundaries are reasonably observed Fig. 8b, as also highlighted by the profiles in Fig. 9d. Note that the experimental FSD image accounts here for the whole sample thickness while the EDP signals only originate from the electron outlet surface [30]. The disorientation map and the associated entrywise norm of the Nye's tensor after subpixel registration (Fig. 8e, f) show that the technique is sensitive to fine details of the microstructure observed in the FSD image (Fig. 8d). As shown by the disorientations map predicted by the CC-based initial guess alone (no IC-GN) in Fig. 8c, the latter can deal with abrupt orientation changes such as the ones highlighted by the disorientation profiles in Fig. 9b.

5. Quantitative analysis and influence of the initial guess

The influence of the initial guess strategy as well as the discrepancies between HTI and DIC disorientation maps are now quantified. To this purpose, three initial guess strategies are tested in the IF steel dataset. The first two are using the CC-based method (FMT-CC + FT-CC), namely the 'partial' initialisation of the homography (i.e. no projective effects, $h_{31} = h_{32} = 0$) and the 'complete' one, respectively. The third approach is HTI based, i.e. all deformation parameters of the homography are initialised according to Eq. (14), where the elastic deformation gradient tensor is approximated by a rotation matrix deduced from the crystallographic orientations as measured by the HTI.

For each one of the $\sim$ 79,000 points composing the dataset, the number of iterations needed for convergence of the IC-GN algorithm is recorded. In addition, the average and the standard deviation of the absolute residuals at the beginning of the IC-GN algorithm (i.e. according to the IG) and at the end (i.e. after the SR) are also recorded. They will be denoted as 'initial' and 'final' residuals in the following, respectively. The "absolute residuals" denote the image formed by the absolute value of the intensity difference between the reference subset and the warped target subset. Note that the reference and the warped target subsets have a mean intensity of 0 with a standard

(a) Disorientation map from HT-based indexation (HTI)

(b) Entrywise norm of the Nye's tensor from HTI

(c) Disorientation map from DIC aided by the CC-based IG

(d) Entrywise norm of the Nye's tensor from DIC

(e) Disorientation map from DIC using the HTI as IG
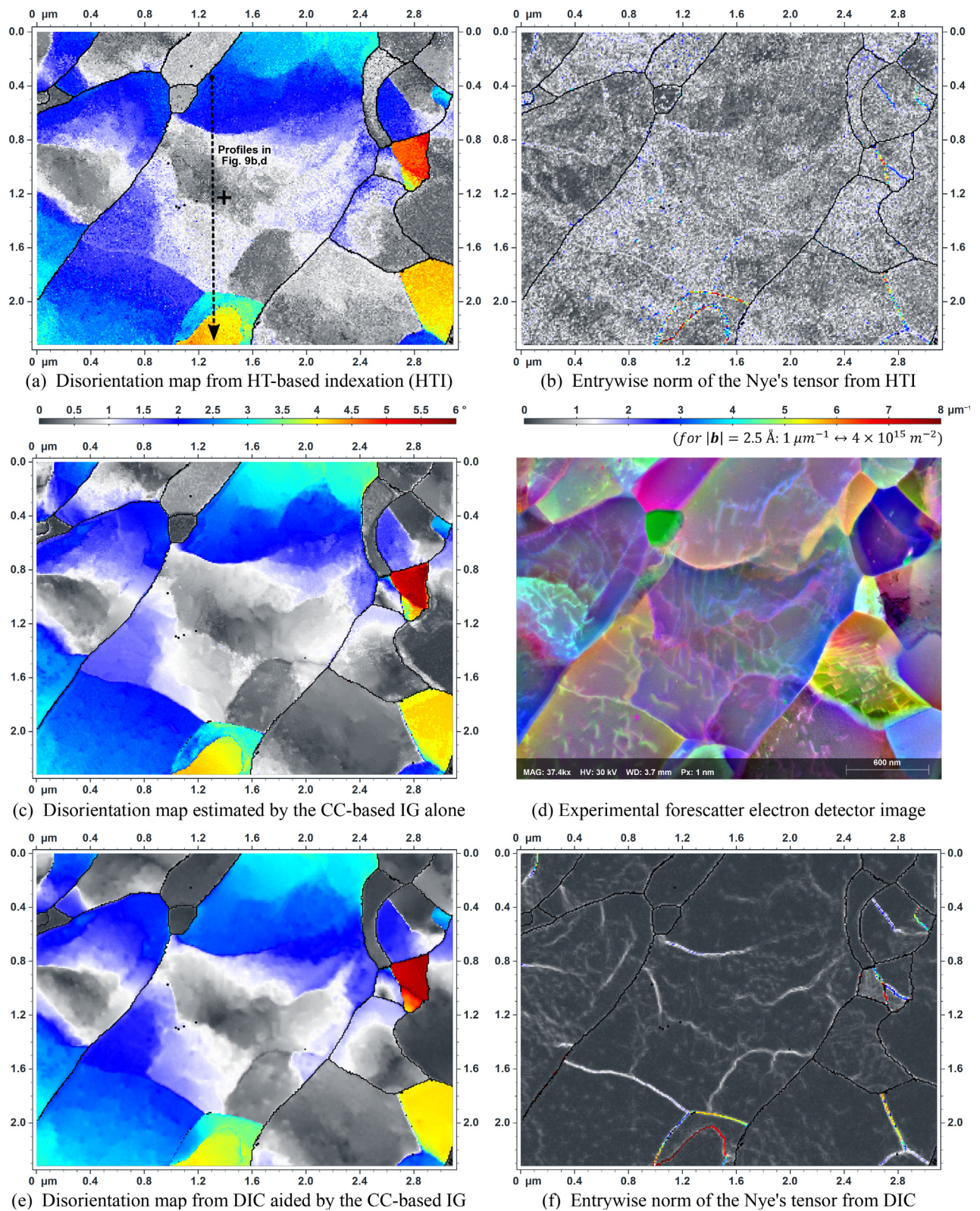
(f) Simulated forescatter electron detector image

Fig. 7. Results in the IF steel. (a) Grain internal disorientation map derived from HTI. Black crosses indicate the location of the patterns shown in Fig. 5. (b) Associated norm of the Nye's tensor. Similarly, (c) and (d) correspond to the results of the DIC analysis which is aided by the proposed CC-based IG while (e) is the disorientation map obtained when using the HTI as IG. To enhance colour variation, disorientation varies from 0° to 8° except within regions delimited by black dash-lines where it goes from 0° up to 12° (f) Simulated FSD image.

deviation of 1 since the C_{ZNSSD} criterion is considered. Such images are extracted from the ODS and IF steel dataset in Fig. 9e-e' and in Fig. 10a, respectively.

Regarding the ODS steel, the examples are taken from a subgrain where the target pattern is disorientated by $\sim 4°$ with respect to the reference. Fig. 9e' shows the final absolute residuals when using the

(a) Disorientation map from HT-based indexation (HTI)

(b) Entrywise norm of the Nye's tensor from HTI

(c) Disorientation map estimated by the CC-based IG alone

(d) Experimental forescatter electron detector image

$(for\ |\boldsymbol{b}| = 2.5\ \text{Å}: 1\ \mu m^{-1} \leftrightarrow 4 \times 10^{15}\ m^{-2})$

(e) Disorientation map from DIC aided by the CC-based IG

(f) Entrywise norm of the Nye's tensor from DIC

Fig. 8. On-axis TKD map in ODS steel. (a) Grain internal disorientation map derived from HTI. The black cross indicates the reference pattern displayed in Fig. 6. (b) Associated norm of the Nye's tensor. Similarly, (e) and (f) correspond to the results of the DIC analysis which is aided by the proposed CC-based IG. (c) Disorientation map estimated by the CC-based IG method alone (no IC-GN). (d) Experimental forecaster electron diffraction image.

'complete' CC-based initial guess. A visual inspection is hard due to the transmitted beam and the diffraction spots left visible on the target while a mask is applied on the reference (Fig. 6c). However, the absolute residuals have a mean value which is twice smaller than

those obtained when warping the target subset according to the HTI alone in Fig. 9e (μ=0.614 vs 1.162). From this standpoint, the disorientation profile from the DIC analysis (black curve in Fig. 9b) is more reliable than the HTI one (red curve), which, in addition to
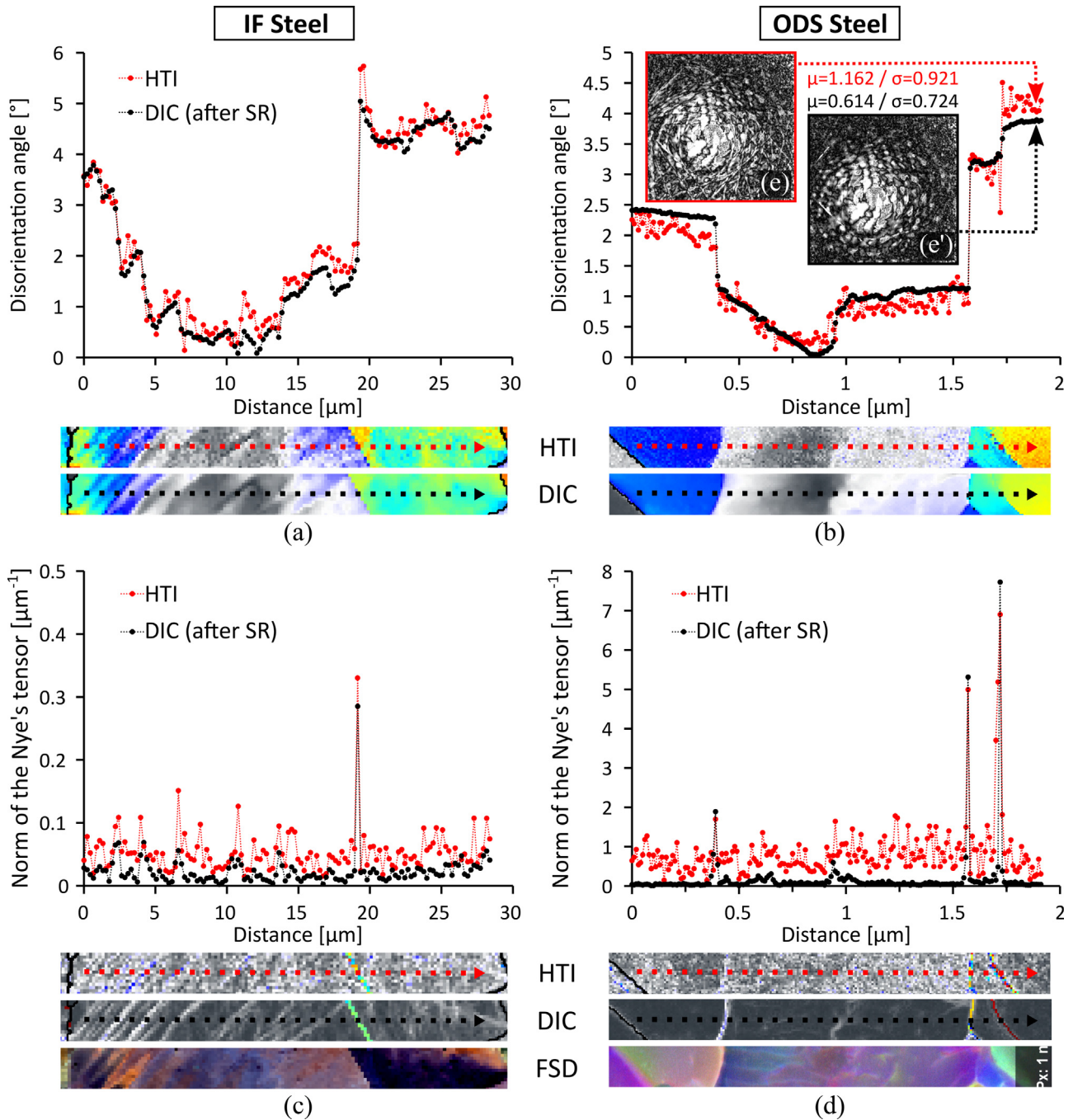
Fig. 9. Profiles of the grain internal disorientations from the HTI and from the DIC analysis in the IF steel (a) and in the ODS steel (b) dataset, whose location is indicated in Fig. 7a and in Fig. 8a, respectively. Similarly, (c) and (d) shows the profiles of the norm of the Nye's tensor. (e) and (e') are the absolute residuals with average value μ and standard deviation σ according to the HTI alone and the DIC analysis aided by the CC-based IG, respectively.

noise, differs by a relatively constant gap of less than 0.5° within the considered subgrain (1.7 to 2 μm). Such a gap can be attributed to an error of the indexing software which is not dedicated for "on-axis" TKD. The band asymmetry is indeed higher in transmission than in reflection (i.e. EBSD) so the HT is more likely to detects excess lines located at band edges rather than the band centres as discussed in [10]. This is why only the IF steel dataset is considered in the following for a fairer comparison with the HTI.

Regarding the IF steel dataset, two of the most disoriented EDP ($\sim$ 12°) are considered in Fig. 10a, which shows the final absolute residuals obtained after SR when using the 'complete' CC-based IG (their frequency distribution is also superimposed on the figure). Its mean value (μ=0.297) and standard deviation (σ=0.269) are typical of the dataset. As indicated indeed by the dotted-arrow lining inset (a) to (b) in Fig. 10, such values correspond to the most encountered cases amongst the dataset (solid black curve). Note that the distributions of the standard deviation of the residuals are not displayed here, but they follow very similar trends than in Fig. 10b. Both the 'complete' and the 'partial' initialisation lead to final absolute residuals having an average of 0.283 and a standard deviation of 0.286, typically. From this standpoint and since no remarkable misalignment is visually observed on the example (Fig. 10a), it arises that the "noise level" within the EDP prevents the average of the absolute residuals to be smaller than $\sim$ 0.2 (Fig. 10b).
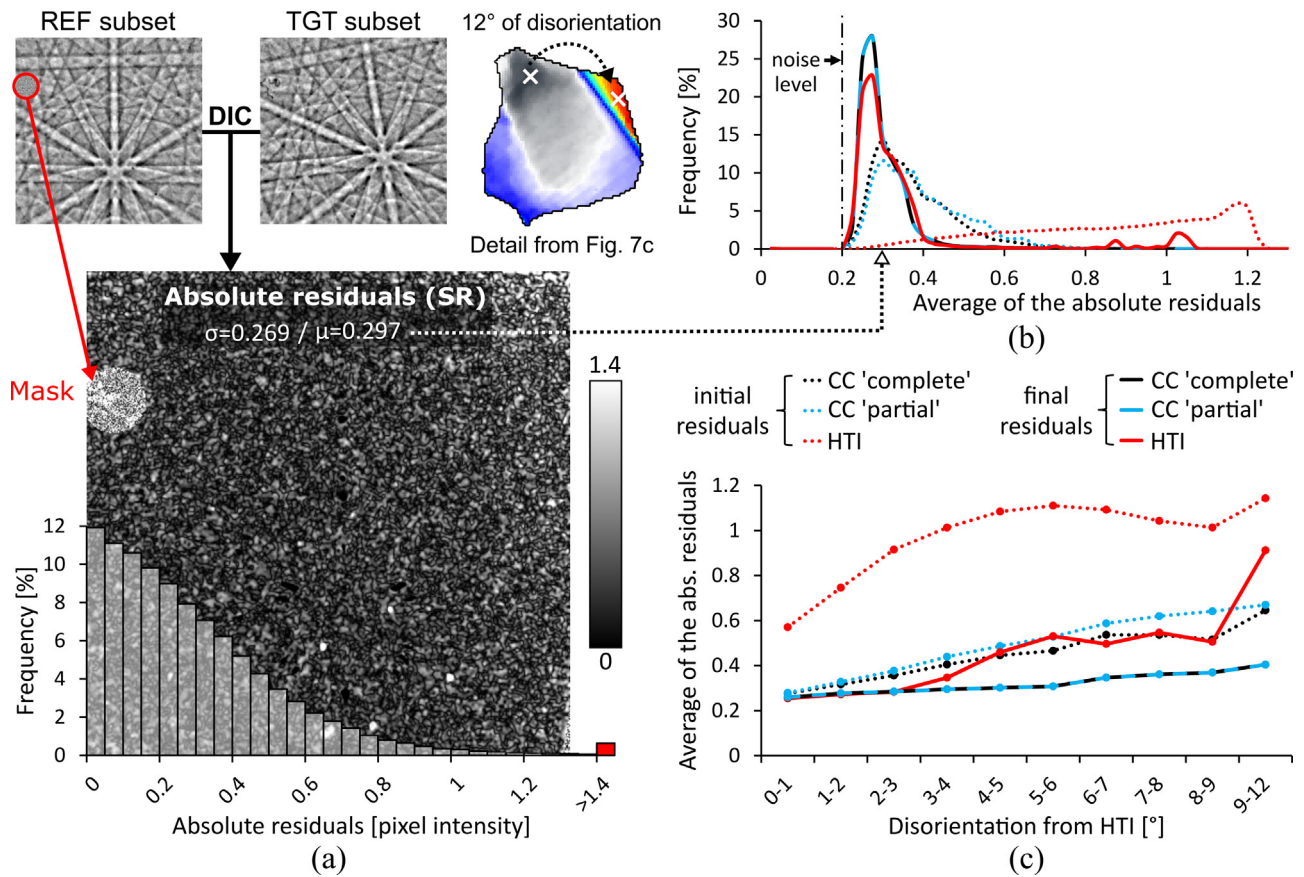
Fig. 10. (a) Absolute residuals after the subpixel registration when aided by the proposed CC-based initial guess, on which their distribution of mean value μ=0.297 and standard deviation σ=0.269 is superimposed. Note that the highest intensities (>1.4) are related to a mask and dust on the scintillator. Here, the considered EDP are two of the most disoriented ones from the IF steel dataset (∼ 12°). (b) Distribution of the average of the absolute residuals before (IG) and after the subpixel registration (SR). (c) Evolution of the average of the absolute residuals as a function of the disorientation.

Besides the distributions in Fig. 10b, the evolution of the average of the residuals as a function of the disorientation angle is plotted in Fig. 10c. As expected, the final residuals (solid curves) are the smallest when the IC-GN algorithm is aided by the CC-based initial guess. Moreover, no noticeable difference is observed between the 'complete' and 'partial' initialisations (black and blue solid lines in Fig. 10c), consistently with the distributions in Fig. 10b. Regarding the initial residuals (dotted lines), the HTI-based initialisation leads to residuals about twice higher than with the proposed CC-based initial guess. Regarding the 'partial' and 'complete' initialisations more precisely, accounting for the projective effects (i.e. h_{31} and h_{32}) results in ∼ 6% smaller initial absolute residuals (distributions in Fig. 10b of mean value 0.384 and 0.361, respectively).

These discrepancies between the three initial guess strategies directly impact the computational efficiency of the IC-GN algorithm. When the CC-based initial guess is used the algorithm indeed converges ∼ 80% faster than with the HTI-based initialisation (75 iterations in average against 40, respectively) as showed in Fig. 11a. This compensates its CPU-time extra-cost, especially since only the points converging in less than 200 iterations are considered here for a fairer comparison (∼260% more iterations otherwise). Regarding the two CC-based strategies more specifically, a 'partial' initialisation lead in average to ∼ 10% more iterations as compared to a 'complete' initialisation (Fig. 11a, grey and blue bar charts). Note that, there is no such a difference between the 'complete' and the 'partial' initialisations in the ODS steel, namely 86 iterations in average with a standard deviation of 26 iterations, for both methods. This is because the on-axis configuration leads to a lower pattern distortion due to the gnomonic projection.

In the IF steel, a convergence in less than 200 iterations concern 99.7% and 90.9% on the dataset when using the CC-based or the HTI-based strategies, respectively. In the first case, the 0.3% discarded points subjected to a slower convergence (i.e. > 200 iterations) display EDP of very poor quality. The convergence issues concern 9.1% of the dataset when using the HTI as IG and importantly, divergence (i.e. > 1000 iterations) even occurs for 4.2% of the dataset as indicated by the black pixels in the disorientation map in Fig. 7e. Such convergence issues are likely to happen as soon as disorientations higher than 3−3.5° are present, which coincides with the appearance of higher final residuals with the HTI-based initialisation as compared to both CC-based ones (Fig. 10c). Both the probability of converging slowly or of diverging and the final residuals significantly worsen with increasing disorientations as showed in Fig. 11b and Fig. 10c, respectively. As the distribution of the disorientation within the whole dataset suggests (black curve in Fig. 11b), there might be a lack of statistics at the highest disorientations, which prevent a clear correlation to be observed. Nevertheless, the number of iterations increases with the disorientation angle for all the investigated strategies in Fig. 11c, consistently with the average of the initial residuals in Fig. 10b.

In order to identify the reasons for this increase and to better assess the influence of the initial guess strategy on the initial residuals, the angular deviation between the HTI-based or the CC-based initial guesses with respect to a reference solution is investigated. Since the true solution is unknown, the result of the DIC aided by the complete CC-based IG is taken as a reference since it minimises the final residuals. Disorientation is characterized either by the disorientation angle and the disorientation axis or by the three rotations
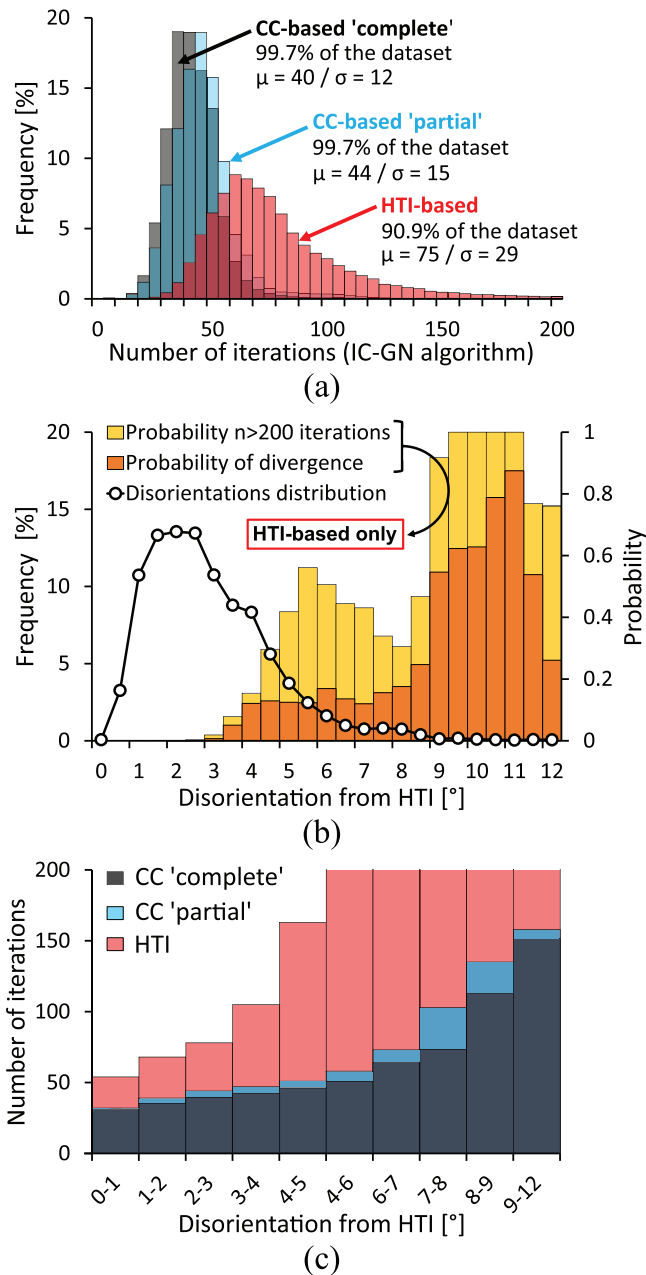
Fig. 11. (a) Distribution of the number of iterations for each initial guess strategy, where μ and σ denote the mean value and the standard deviation of the distributions, respectively. (b) Distribution of the disorientation angles from HT within the whole dataset (black curve) and probabilities of converging slowly (>200 iterations) or of diverging (>1000 iterations) as a function of the disorientation angle when using the HTI-based initialisation. (c) Mean number of iterations of the IC-GN algorithm as a function of the disorientation angle for all the IG strategies.

around the axes of the sample frame. The second representation is used below and the angular deviations on the three rotation components w_i are computed pointwise over the whole dataset. The rotation components and the disorientations according to the CC-based initial guess alone are deduced from Eq. (10) considering the 'complete' initialisation of the homography in Eq. (14). No difference should be made between the 'partial' and the 'complete' initialisations. Indeed, they lead to a different warping of the initial target pattern, but the disorientations deduced from the FMT-CC and FT-CC analysis are the same.

The distributions of the angular deviations with respect to the SR aided by the CC-based IG in Fig. 12a show that the lattice rotations

estimated by the HTI-based analysis are 4–5 times more scattered than for the CC-based initial guess (1–1.2° and 0.2–0.3°, respectively). Such a scattering in the rotation components involved in the calculation of the GND densities is the cause of the very noisy GND map in Figs. 7b and 8b. It is also consistent with the wider spread in the distribution of the average of the initial absolute residuals when using the HTI-based initialisation in Fig. 10b (red dotted curve), as compared to both CC-based strategies (black and blue dotted curves). Note that the angular deviation regarding the rotation around $\vec{X_3}$ (Fig. 12a) has a standard deviation that is ∼ 50% higher than for the other axes (0.31° in comparison with ∼ 0.2°). This is related to the angular resolution of the FMT-CC, namely 0.35° here (180°/512 pixels), which is slightly improved by fitting the peak of the cross-correlation function. If the resolution could be improved by using higher-resolution EDP, its present performances remain nevertheless sufficient to ensure a good convergence of the IC-GN algorithm as compared to the HTI-based initialisation (Fig. 11).

Besides the scattering of the values, the evolution of the angular deviation with the disorientation angles in Fig. 12b follows exactly the same tendencies than the average of the initial residuals in Fig. 10c, confirming the higher accuracy of the CC-based initial guess on the lattice rotations. Interestingly, the HTI presents smaller angular deviations at small disorientations, where the uncertainty on the disorientation axis is expected to be the highest [63]. It is observed that the convergence issues occurring above 3–3.5° when using the HTI-based initialisation (Fig. 11b) actually correspond to the disorientation range for which angular deviations are greater than 1° in Fig. 12b. On the one hand, this is in agreement with previous works [32,33]. On the other hand, this confirms that the HTI cannot provide a suitable initial guess in a systematic way, as already suggested in section 2.3 before proposing the CC-based approach. Further investigations also reveal that all diverging points when using the HTI-based initialisation actually admit an angular deviation of more than 2° on at least one of the estimated rotation component, which never happens with the CC-based initial guess.

Finally, it is worth noting that both the number of iterations and the residuals (initial and final) increase with the disorientation angle while the angular deviations of each initial guess strategy remains relatively constant for disorientations higher than 5° in Fig. 12b. Therefore, the increases observed in Figs. 11c and 10c cannot be attributed to the initial guess alone. Indeed, the warped target subset may partially disappear from the EDP or at least, it may contain an increasing amount of near-edges regions with a lower signal-to-noise ratio. The variation of the band contrast with the orientation can also play a role, as raised in [25].

In brief, the CC-based IG ensures a higher computation efficiency of the IC-GN algorithm as compared to a HTI-based initialisation, in particular at high disorientations (>4°). Moreover, neglecting the projective effects when conducting the FMT-CC + FT-CC measurements and when warping the initial target subset appears to be a reasonable assumption for the investigated range of disorientations, as already suggested in Fig. 5. If the 'complete' initialisation should be preferred for computational efficiency, the 'partial' one makes the DIC analysis fully independent from the SEM calibration since even a coarse knowledge of the SEM calibration is not required for the initial guess.

6. Discussion

Borrowing techniques in the field of experimental mechanics, a 'global' DIC approach for rotation and elastic strain measurement from EDP is proposed. Subpixel registration is performed by a state-of-the-art IC-GN algorithm analysing EDP as a whole through a unique and large ROI. The working principle is thus similar to recent but independent works [32,34], which tends to reinforce our choices. The implementation however differs. First, relative deformations of
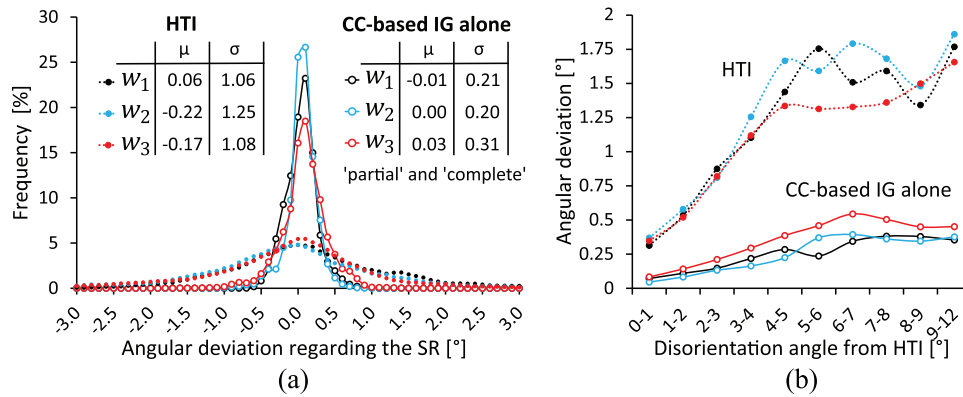
Fig. 12. (a) Distribution of the angular deviations of the rotation components estimated by the CC-based IG and by the HT-based indexation (HTI), where μ and σ denote the mean value and the standard deviation of each distribution, respectively. (b) Evolution of the angular deviation as a function of the disorientation angle. Deviations are measured with respect to the DIC aided by the 'complete' CC-based IG (Fig. 7c), which minimizes at best the final residuals.

the ROI are described by a first-order homography, independently from the SEM calibration. Second, it accounts for optical distortions without substantially impacting the numerical cost of the analysis.

As demonstrated in section 2.1, a linear homography enables to recover the deviatoric deformation gradient tensor while offering the possibility of an 'uncoupled' DIC approach. Yet, Ruggles et al. [33] justified the development of an 'integrated' DIC approach (i.e. where the DIC and the SEM calibration are coupled) by stating that no linear (or even quadratic) shape function is appropriate for HR-EBSD. Their reasoning is apparently linked to the consideration of Euclidian coordinates. As shown here however, this is not a requirement and homogeneous coordinates, often met in the field of computer vision to deal with projective transformations, can be used.

If the development of an 'uncoupled' method is first historical, it was maintained despite the emergence of several I-DIC approaches [32,34] for the following reasons:

(i) Certainly, an 'uncoupled' approach implies additional steps (i.e. Eqs. (8) and (10)) to deduce the deformation gradient tensor. However, they do not introduce error apart from numerical approximations inherent to floating point calculation, which are negligible when compared to both DIC and calibration uncertainties.

(ii) The error made by the DIC is separated from the calibration uncertainty. If calibration is modified, a dataset is re-analysable in a negligible time-lapse. Indeed, the analysis will directly start from Eq. (8) where the deformation parameters h_{ij} are already known.

(iii) The numerical cost of the above mentioned additional steps is largely compensated during the GN algorithm which is from our point of view simpler to implement. There is no need to pre-process the patterns in order to compensate the variations of the calibration parameters [34] or to account for them when computing each warped coordinates [33]. Instead, the latter are computed in a compact way in Eq. (7) and the deformation parameters are corrected using Eq. (8) only once per EDP. Moreover, the locations ξ (or $\hat{\xi}$) remain also unchanged during the whole analysis, saving the computation of the relative position of each points with respect to the (displacing) pattern centre.

It must nevertheless be recognised that I-DIC is at some point particularly convenient. The deformation parameters are directly the components of the deviatoric deformation gradient tensor, which undoubtedly eases the initialisation of the GN algorithm, the understanding of its underlying equations or the interpretation of its results. This is especially appreciable when considering potential cross-grain analyses [35].

The performances are tested using the standard EBSD technique as well as the newly developed on-axis TKD configuration for which a global DIC approach is applied for the first time. This echoes the recent works by Yu et al. [28] and Tang et al. [29], who first applied the 'local' HR-EBSD technique to "off-axis" and "on-axis" TKD, respectively. Besides the investigated techniques, another originality of this work also stems from the chosen materials, whose thermomechanical treatments have caused significant plastic strains. Indeed, the HR-EBSD technique mainly focusses on the measurement of elastic strains, which is particularly relevant in purely elastically or slightly plastically deformed materials. As an example, experimental applications of the recent "global" HR-EBSD have only been carried out by Shi et al. [34] to our knowledge. After validating their approach by bending a silicon single crystal, the authors assessed the elastic strains in an austenitic steel deformed at the onset of plasticity, with an impressive uncertainty of $\sim 4.10^{-5}$ where slip is not activated.

Here, the investigated 15% strained IF steel sheet and the quenched and tempered ODS steel thin foil are representative of engineering problems, for which plastic strains are important as compared to elastic strains (the latter are also negligible as compared to elastic curvatures when estimating the Nye's tensor). They are commonly analysed by means of the HT-based indexation although it misses most of the dislocation structures, in particular at the low disorientations, as illustrated in Fig. 7b and Fig. 8b. Despite it is not a novelty, such markedly deformed and polycrystalline materials remain underexplored by high-angular resolution techniques. Only a few studies like the one by Jiang et al. [62] are available in the literature. A major reason is the drop of accuracy due to the deterioration of the pattern quality, aggravated by high rotations. Accurate calibration which is still an active research area in of the HR-EBSD community, is also affected as evidenced by Tanaka & Wilkinson [58], where the accuracy of the proposed pattern matching analysis worsens in deformed regions of the investigated IF steel specimen. Calibration may be perfectible in the present work but requires scientific and technical developments.

Despite all of this, the results suggest that the HR-EBSD technique can be applied to a larger range of materials, complementary to recent indexation techniques [13,16]. Relatively large regions are characterized in Figs. 7 and 8 using standard cameras mounted on a SEM tailored for imaging which lacks stability. Comparison with experimental or simulated FSD images indicates that the DIC faithfully highlights details of the microstructure. In the examples shown here the elastic strains may be questionable mainly because of insufficient calibration. As mentioned in section 3.2, 'phantom' strains are possibly present so the elastic strains in ODS steel displayed in Fig. 13 are rather qualitative. As the material contains nano-sized oxide precipitates near the surface, the stress free surface assumption is not considered here. Only five elastic strains components are consequently shown in Fig. 13a-e. They are obtained by polar decomposition of the deviatoric deformation
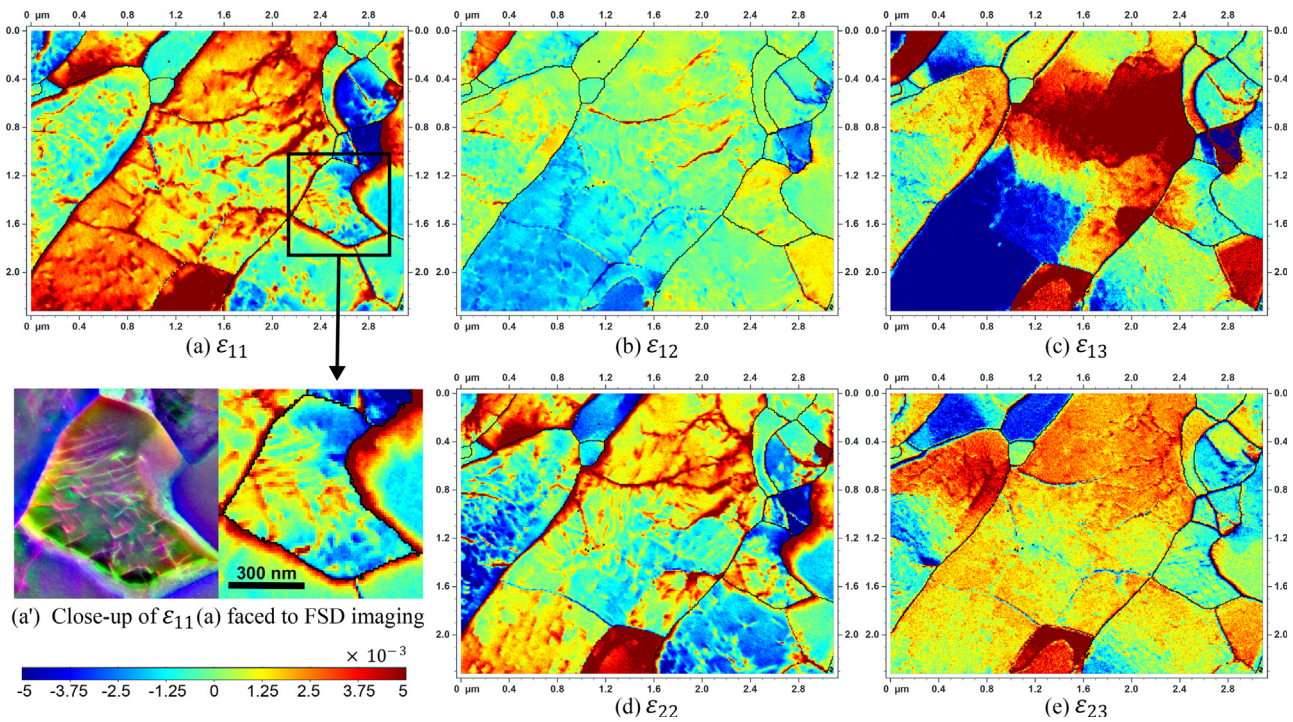
Fig. 13. Elastic strain mapping in the ODS steel obtained by the 'global' DIC approach aided by the CC-based IG with complete initialisation of the homography.

gradient tensor expressed in the sample frame. In the light of the close-up in Fig. 13a' of the elastic strain mapping of ε_{11}, the method seems very promising. Thanks to the 10 nm step size, features corresponding to single dislocations according to the experimental FSD image are clearly visible within the elastic strain field.

Several aspects of the proposed method can be improved. Analysis speed can be enhanced as the IC-GN algorithm is parallelizable [64] and possible optimisations are addressed in [54,55]. Besides, both IC-GN and FA-GN algorithms are benefiting from tremendous developments like in a very recent work by Su et al. [65] where systematic error is significantly reduced by applying random offsets to sampling positions. Instead of using computationally demanding biquintic B-splines (whose extra cost as compared to cubic ones is already questioned by Ruggles et al. [33]), lower order interpolation schemes could be used without loss of accuracy. Robustness against noise or pattern blurring can be enhanced by means of error functions [66]. As far as the initial guess is concerned, the FMT is currently approximated but an analytical computation is also possible as reviewed [67]. More generally, the initial guess strategy can be optimised by coupling the present path independent method with a reliability guided and path dependant one. Indeed, the proposed CC-based initial guess can be only use when an initialisation of the homography from the neighbouring points fails to ensure a satisfying convergence of the IC-GN algorithm.

Finally, the convergence properties of the 'global' HR-EBSD technique should be clarified. The accuracy of the initial guess is known to be determinant on the efficiency of the GN-algorithm [37,38], which has been highlighted by using simulated patterns in [32,33]. Here, the use of an automated CC-based initial guess ensures an 80% faster convergence of the IC-GN algorithm than when considering the HTI-based indexation, for which divergence predominantly occurs for larger disorientations. Since the GN-algorithm is a local optimisation scheme, it is primordial to ensure that it converges towards the correct solution. Besides the convergence radius, the convergence criterion is another essential factor [38]. As investigated by Pan et al. [56] for speckle patterns, the latter should neither be too loose nor too stringent such that the optimum ratio between accuracy and computational efficiency is obtained.

7. Conclusions

- A first-order homography applied to a unique and large subset allows electron diffraction patterns to be registered independently from the SEM calibration. In this novel global HR-EBSD/HR-TKD framework, the calibration is only considered afterwards to deduce the lattice rotations and elastic strains from the DIC measurements.
- The crystallographic orientations obtained by the Hough-transform based indexation are not precise enough to correctly initialise the IC-GN algorithm. Large disorientations or discontinuities can be resolved by the IC-GN algorithm with the help of a cross-correlation based initial guess (FMT-CC + FFT-CC). The latter pre-aligns pattern disoriented here up to 23° in an automated and path-independent way. Moreover, the estimation of the lattice rotations is sufficiently fine to ensure the IC-GN algorithm to convergence efficiently, here up to 12°
- Despite the medium resolution of the electron diffraction patterns and the thermomechanical states of the studied material which deteriorates their quality, the proposed DIC analysis appears sufficiently robust and sensitive to provide a fine description of the grain internal disorientations and GND densities. This suggests that various engineering microstructures classically investigated by standard indexation techniques could benefit from the present HR-EBSD/HR-TKD technique.

Appendix A. Correction of the deformation parameters of the homography

The effects of the variation of the projection geometry can be modelled by the matrices T in Eq. (A.1) and S in Eq. (A.2), which describe a uniform translation by a vector $(\Delta_1^{PC} \quad \Delta_2^{PC})^T$ and an

isotropic scale by a factor α with respect to the pattern centre of the reference pattern, respectively. Note that the translational part in Eq. (A.2) reflects the fact the centre of the homography $\boldsymbol{X_0}$ does not necessary coincide with the pattern centre. The corrected deformation parameters $\widehat{h}_{ij}$ are deduced from the ones measured by the DIC (h_{ij}) by multiplying $(S.T)^{-1}$ by the homography in Eq. (5), which immediately leads to the relationships in Eq. (8).

$$T = \begin{pmatrix} 1 & 0 & \Delta_1^{PC} \\ 0 & 1 & \Delta_2^{PC} \\ 0 & 0 & 1 \end{pmatrix} \tag{A.1}$$

$$S = \begin{pmatrix} \alpha & 0 & x_{01}.(\alpha-1) \\ 0 & \alpha & x_{02}.(\alpha-1) \\ 0 & 0 & 1 \end{pmatrix} \tag{A.2}$$

Appendix B. Relationships between the homography and the deviatoric deformation gradient

In the following, a two-component vector gives a position on the scintillator in 2D Euclidian coordinates (EC) while a three-component vector is a representation of such a 2D point in homogeneous coordinates (HC). By definition, $\boldsymbol{\xi} = \boldsymbol{X} - \boldsymbol{X}_0$ where $\boldsymbol{X}_0$ is the geometric centre of the ROI, located at $(x_{01} \quad x_{02})^T$ with respect to the pattern centre (of the reference). A possible representation of ξ in HC is $(x_1 - x_{01} \quad x_2 - x_{02} \quad 1)^T$. Starting from Eq. (3), it leads to

$$\begin{pmatrix} \xi_1' \\ \xi_2' \\ \xi_3' \end{pmatrix} = \begin{pmatrix} (1+h_{11}).x_1 + h_{12}.x_2 + h_{13} - (h_{11}+1).x_{01} - h_{12}.x_{02} \\ h_{21}.x_1 + (1+h_{22}).x_2 + h_{23} - h_{21}.x_{01} - (1+h_{22}).x_{02} \\ h_{31}.x_1 + h_{32}.x_2 + 1 - h_{31}.x_{01} - h_{32}.x_{02} \end{pmatrix}. \tag{B.1}$$

By multiplying its right side by $DD/(1 - h_{31}.x_{01} - h_{32}.x_{02})$ according to the 'homogeneous property' (Eq. (6)), Eq. (B.1) is rearranged as follows:

$$\begin{pmatrix} \xi_1' \\ \xi_2' \\ \xi_3' \end{pmatrix} = \begin{pmatrix} DD.\left[\frac{1+h_{11}}{1-h_{31}.x_{01}-h_{32}.x_{02}}.x_1 + \frac{h_{12}}{1-h_{31}.x_{01}-h_{32}.x_{02}}.x_2 + \frac{h_{13}-(1+h_{11}).x_{01}-h_{12}.x_{02}}{DD.(1-h_{31}.x_{01}-h_{32}.x_{02})}.DD\right] \\ DD.\left[\frac{h_{21}}{1-h_{31}.x_{01}-h_{32}.x_{02}}.x_1 + \frac{1+h_{22}}{1-h_{31}.x_{01}-h_{32}.x_{02}}.x_2 + \frac{h_{23}-h_{21}.x_{01}-(1+h_{22}).x_{02}}{DD.(1-h_{31}.x_{01}-h_{32}.x_{02})}.DD\right] \\ \frac{DD.h_{31}}{1-h_{31}.x_{01}-h_{32}.x_{02}}.x_1 + \frac{DD.h_{32}}{1-h_{31}.x_{01}-h_{32}.x_{02}}.x_2 + DD \end{pmatrix}. \tag{B.2}$$

The third homogenous component is assumed non-zero and all components are consequently divided by the latter to get back to EC (i.e. $\xi_1' = x_1' - x_{01}$ and $\xi_2' = x_2' - x_{02}$):

$$\begin{pmatrix} x_1' - x_{01} \\ x_2' - x_{02} \end{pmatrix} =$$

$$\begin{pmatrix} DD.\frac{\left[\frac{1+h_{11}}{1-h_{31}.x_{01}-h_{32}.x_{02}}.x_1 + \frac{h_{12}}{1-h_{31}.x_{01}-h_{32}.x_{02}}.x_2 + \frac{h_{13}-(1+h_{11}).x_{01}-h_{12}.x_{02}}{DD.(1-h_{31}.x_{01}-h_{32}.x_{02})}.DD\right]}{\frac{DD.h_{31}}{1-h_{31}.x_{01}-h_{32}.x_{02}}.x_1 + \frac{DD.h_{32}}{1-h_{31}.x_{01}-h_{32}.x_{02}}.x_2 + DD} \\ DD.\frac{\left[\frac{h_{21}}{1-h_{31}.x_{01}-h_{32}.x_{02}}.x_1 + \frac{1+h_{22}}{1-h_{31}.x_{01}-h_{32}.x_{02}}.x_2 + \frac{h_{23}-h_{21}.x_{01}-(1+h_{22}).x_{02}}{DD.(1-h_{31}.x_{01}-h_{32}.x_{02})}.DD\right]}{\frac{DD.h_{31}}{1-h_{31}.x_{01}-h_{32}.x_{02}}.x_1 + \frac{DD.h_{32}}{1-h_{31}.x_{01}-h_{32}.x_{02}}.x_2 + DD} \end{pmatrix} \tag{B.3}$$

The deformed coordinates x_i' are isolated by passing the offsets x_{01} and x_{02} on the right side which leads to:

$$\begin{pmatrix} x_1' \\ x_2' \end{pmatrix} =$$

$$\begin{pmatrix} DD.\frac{\left[\frac{1+h_{11}+h_{31}.x_{01}}{1-h_{31}.x_{01}-h_{32}.x_{02}}.x_1 + \frac{h_{12}+h_{32}.x_{01}}{1-h_{31}.x_{01}-h_{32}.x_{02}}.x_2 + \frac{1}{DD}\left(\frac{h_{13}-(1+h_{11}).x_{01}-h_{12}.x_{02}}{1-h_{31}.x_{01}-h_{32}.x_{02}}+x_{01}\right).DD\right]}{\frac{DD.h_{31}}{1-h_{31}.x_{01}-h_{32}.x_{02}}.x_1 + \frac{DD.h_{32}}{1-h_{31}.x_{01}-h_{32}.x_{02}}.x_2 + DD} \\ DD.\frac{\left[\frac{h_{21}+h_{31}.x_{02}}{1-h_{31}.x_{01}-h_{32}.x_{02}}.x_1 + \frac{1+h_{22}+h_{32}.x_{02}}{1-h_{31}.x_{01}-h_{32}.x_{02}}.x_2 + \frac{1}{DD}\left(\frac{h_{23}-h_{21}.x_{01}-(1+h_{22}).x_{02}}{1-h_{31}.x_{01}-h_{32}.x_{02}}+x_{02}\right).DD\right]}{\frac{DD.h_{31}}{1-h_{31}.x_{01}-h_{32}.x_{02}}.x_1 + \frac{DD.h_{32}}{1-h_{31}.x_{01}-h_{32}.x_{02}}.x_2 + DD} \end{pmatrix} \tag{B.4}$$

Finally, a term-by-term comparison of Eq. (B.4) with the HR-EBSD problem in Eq. (9) directly gives the relationships in Eq. (10).

Appendix C. Detail and illustration and of the working principle of the initial guess

The translation of a reference ROI $\widetilde{r}$ leading to the highest similarity with a target ROI $\widetilde{t}$ according to the C_{ZNCC} criterion is measured by localizing the maximum of the normalised cross-correlation function (XCF) with respect to its centre. According to the Fourier shift theorem, such this spatial translation generates a phase shift between the FT. Based on this, FT-CC is a numerically efficient FFT-based peak finding algorithm which computes the normalised XCF as follows:

$$XCF = \Im^{-1}\left\{ \frac{\Im^*\{\widetilde{r}\}.\Im\{\widetilde{t}\}}{\left|\Im^*\{\widetilde{r}\}\right|.\left|\Im\{\widetilde{t}\}\right|} \right\}, \tag{C.1}$$

where $\Im$, $\Im^*$ and $\Im^{-1}$ denote the FT, its conjugate and its inverse, respectively. FT-CC is however unsuitable for images rotated by more than $6-8°$ or whose scale factor is not close to 1 [47]. If the second case is never happening when working with EDP, harmful effects of rotation have already been pointed out by Maurice et al. [25] and Britton et al. [24] as they proposed the remapping technique. The FMT uncouples the spatial effects of rotation and scaling from translation such that the latter results in phase shift between the FMT [67−69]. Rotation and scale are consequently measured despite the presence of translation by means of FMT-CC, i.e. using the FMT instead of the FT in Eq. (C.1).

The on-axis TKD patterns from Fig. 5 are used to illustrate the working principle of the method in the following. There is about $-18°$ in-plane rotation between these two 600×600 px^2 EDP (Fig. C1a,a'). A Kikuchi band is highlighted in red to make it more readily visible. In practise, a reduced ROI of 512×512 px^2 is considered in order to allow a direct use of FFT algorithms and because the signal is particularly noisy on edges. The latter is windowed with a cosine-tapered function (Fig. C1b,b') to prevent spectrum leakage while computing the FT (Fig. C1c,c'). As the window w is applied to the signal s, the average intensity of the windowed signal $\widehat{s}$ is simultaneously brought to zero according to:

$$\widehat{s}(\boldsymbol{\xi}) = \left(s(\boldsymbol{\xi}) - \frac{mean(s.w)}{mean(s)}\right).w(\boldsymbol{\xi}) \tag{C.2}$$

(i.e. $\widetilde{r}$ and $\widetilde{t}$ are replaced by $\widehat{r}$ and $\widehat{t}$ in Eq. (C.1). As expected, a direct FT-CC analysis fails to recover the translation because the XCF (Fig. C1g) contains plenty of peaks of relatively similar intensity. FMT-CC is thus conducted first.

In order to compute the FMT, a method proposed by Reddy & Chatterji [69] is adopted here because of its easy implementation. It consists in a resampling of the log-amplitude of the FT in a polar or log-polar frame and the FT is then computed in order to obtain the FMT. Actually, a polar frame is sufficient since negligible scale changes are expected. This makes rotation and scale visible in the form of vertical and horizontal translations in Fig. C1d,d', respectively. The resampled coordinates are read from a pre-computed look-up table to avoid redundant calculations while interpolation is performed according to a 3-points bilinear scheme [70] avoiding the "checkerboard" effect of conventional 4-points bilinear interpolation. The FMT is then obtained by computing the FT (Fig. C1e,e') from which the XCF is deduced by FMT-CC (Fig. C1f). The in-plane rotation angle θ_3 is deduced from its clear peak indicated by the red shift, as detailed in [47,69]. In order to lower the calculation effort, the scale factor is assumed equal to 1 such that the steps from Fig. C1d,e and f are actually reduced to a 1-dimension signal although 2-dimensional images are used here for illustration purpose. More precisely, Fig. C1d,d' can be replaced by a 1D-array containing the average value of each row. Note that this approach is at some point similar with a recent work by Foden et al. [71] where the authors perform a log-polar resampling of the spatial images instead of the magnitude of their FT in order to measure the in-plane rotation. This is because those images only differ
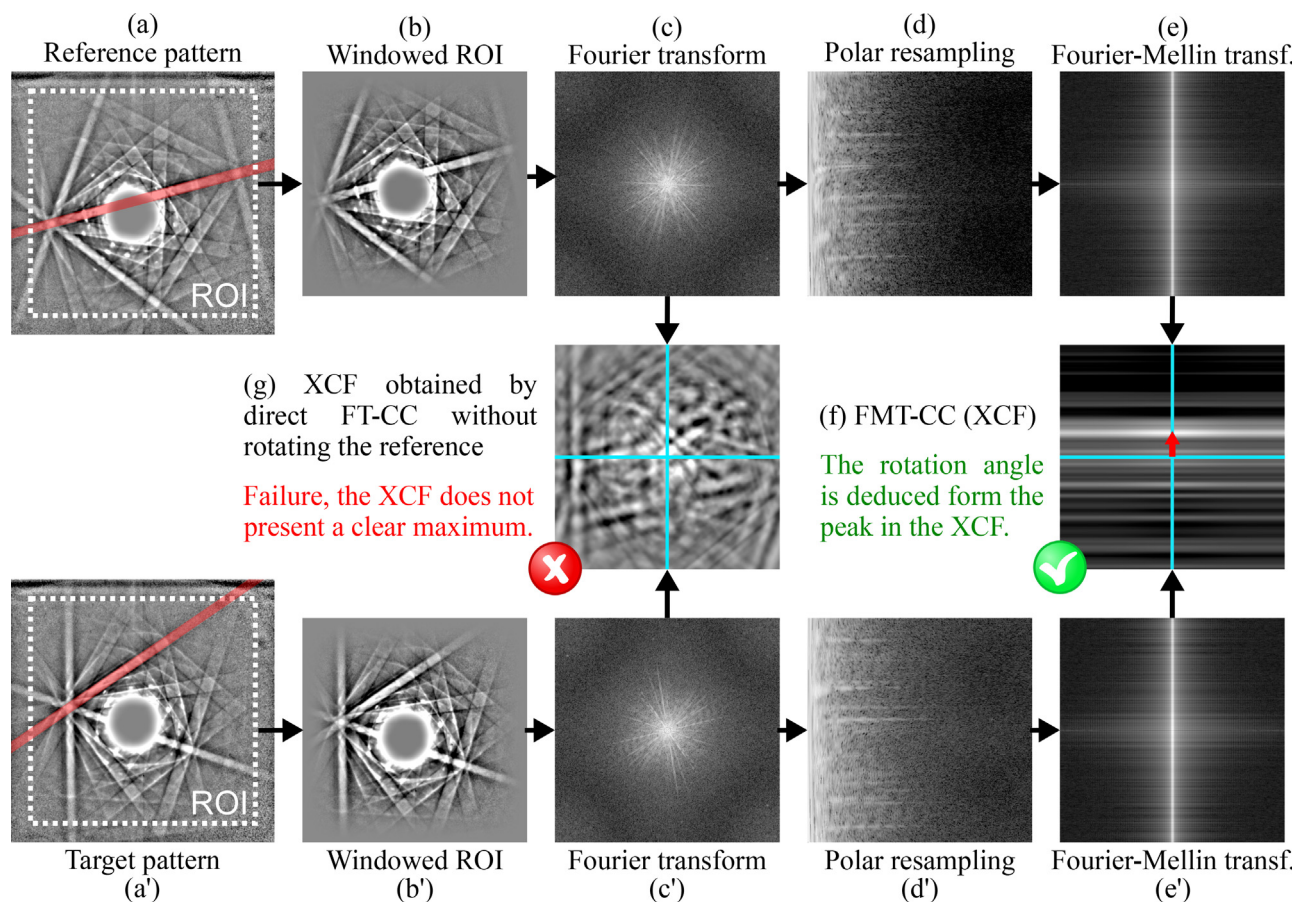
Fig. C1. Working principle of the in-plane rotation estimation by means of FMT-CC. (a) Reference pattern. Similarly, prime refers to the target image. (b) Windowed ROI. (c) FT of (b) in Cartesian coordinates. (d) Resampling of the log-magnitude of (c) in a polar frame. (e) FT of (d) after replacing each row by its average value. (f) XCF obtained by FMT-CC. A clear peak downwards the XCF centre indicates that in-plane rotation is present. The rotation angle θ_3 is deduced from the vertical red shift. (g) XCF obtained by direct FT-CC of the windowed ROI. Since large in-plane rotation is present, no clear peak is observed within the XCF and in-plane translation cannot be reliably measured.
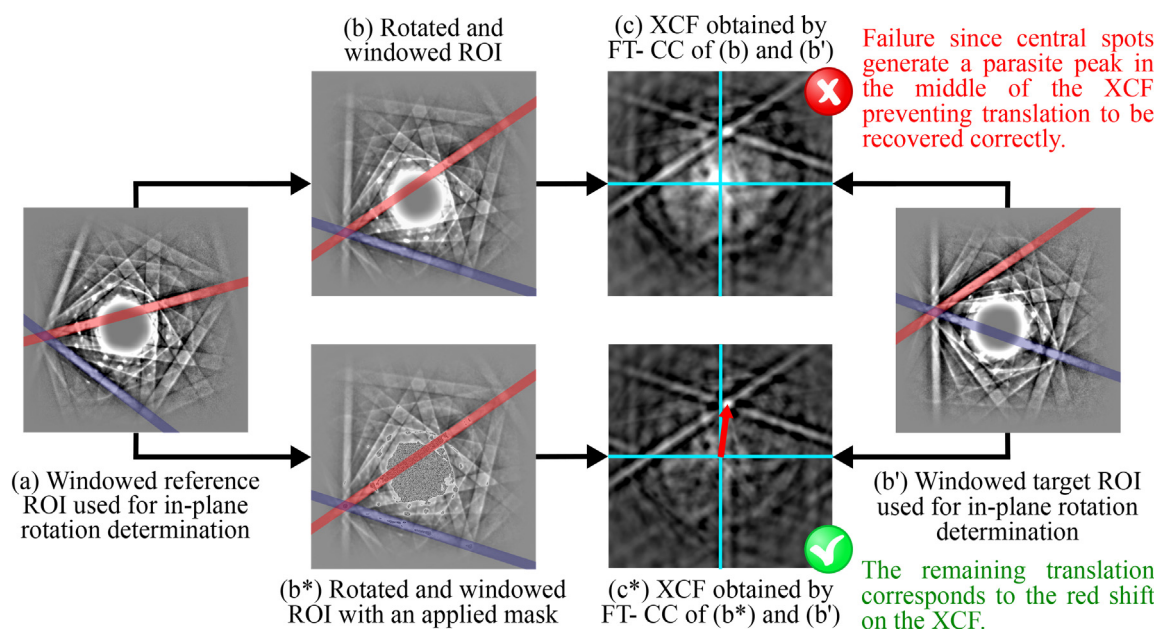
Fig. C2. Working principle of the determination of the remaining in-plane translation by means of FT-CC. (a) Windowed reference ROI used during FMT-CC. (b) Reference ROI rotated by θ_3 and windowed. (b*) Same ROI than (b) but with an applied mask on the central spot. (b') Windowed target ROI used during FMT-CC. (c) XCF obtained by FT-CC of (b) and (b'). Translation fails to be recovered because of a parasite peak in the middle of the XC due to the transmitted beam. (c*) FT-CC of (b*) and (b'). The XCF has a clear peak and the arrow corresponds to the remaining translation.

by a rotation around their centre which must coincide with the pattern centre. It is not necessary the case here. More generally, different ways exist to compute a FMT [67] so that the polar resampling can be avoided.

The reference ROI is rotated around its centre $\boldsymbol{X}_0$ by $\theta_3 = -18°$ (Fig. C2b,b*) while the target ROI remains unchanged (Fig. C2b' is the same than Fig. C1b') and the remaining translation is measured by FT-CC. This is however expected to fail in the case of on-axis TKD because of the transmitted beam, i.e. the saturated central spot. It works as an "anchor" by generating a parasite peak in the middle of the XCF (Fig. C2c). The latter is consequently hidden by applying a mask on the reference (Fig. C2b*). The so-obtained. XCF (Fig. C2c*) has then a clearly identifiable peak from which the remaining translation $\overrightarrow{\Delta}$ is deduced. Here, the latter is about $\Delta x_1 = 10$ and $\Delta x_2 = -118$ pixels along $\overrightarrow{X_1}$ and $\overrightarrow{X_2}$, respectively. Note that in practice, the XCF peak are fitted with a Gaussian similarly to the 'local' HR-EBSD technique [21] in order to enhance the resolution of the technique.

Appendix D. Implementation of the IC-GN algorithm

For the proposed parametrization of the homography, the Jacobian is given as a function of $\boldsymbol{p}$ in Eq. (D.1). The convergence criterion is defined according to Eq. (D.2) which is inspired from [55].

$$\boldsymbol{J}_W(\boldsymbol{\xi},\boldsymbol{p}) = \frac{1}{h_{31}.\xi_1 + h_{32}.\xi_2 + 1} \begin{pmatrix} \xi_1 & \xi_2 & 1 & 0 & 0 & 0 & -\xi_1.\xi_1' & -\xi_2.\xi_1' \\ 0 & 0 & 0 & \xi_1 & \xi_2 & 1 & -\xi_1.\xi_2' & -\xi_2.\xi_2' \end{pmatrix}$$
(D.1)

$$\sqrt{\sum_{i=1}^{2}\sum_{j=1}^{3}\left(\Delta h_{ij}.\xi_{j_{max}}\right)^2 + \left(\Delta h_{31}.\xi_{1max}\right)^2 + \left(\Delta h_{32}.\xi_{2max}\right)^2} < 0.001$$

$$where \quad \xi_{j_{max}} = \begin{cases} max(\xi_1) & if\ j=1 \\ max(\xi_2) & if\ j=2 \\ 1 & if\ j=3 \end{cases}$$
(D.2)

Appendix E. High-pass log filtering

Let $I(x, y) \geq 0$ be the grey intensity at location (x, y) within the pattern. The high-pass log filter is applied according to Eq. (E.1). $\widetilde{I}(x, y)$ is the filtered intensity and $N = 2k + 1$ is the size of the kernel. Equation corresponds to the general case. Image can be padded by repeating borders in order to deal with edges.

$$\widetilde{I}(x,y) = N^2.log[\ I(x,y)+1\ ] - \sum_{i=-k}^{k}\sum_{j=-k}^{k}log[\ I(x+i,y+j)+1\ ]$$
(E.1)

References

[1] B.L. Adams, S.I. Wright, K. Kunze, Orientation imaging: the emergence of a new microscopy, Metall. Trans. A. 24 (1993) 819–831, doi: 10.1007/BF02656503.

[2] S.I. Wright, A review of automated orientation imaging microscopy (OIM), J. Computer-Assisted Microscopy 5 (1993) 207–221.

[3] R.A. Schwarzer, Present state of electron backscatter diffraction and prospective developments, in: D.P. Field, B.L. Adams, M. Kumar, A.J. Schwartz (Eds.), Electron Backscatter Diffraction in Materials Science, 2nd ed.Springer US, 2009, pp. 1–20, doi: 10.1007/978-1-4757-3205-4_1.

[4] D. Chen, J.-.C. Kuo, W.-.T. Wu, Effect of microscopic parameters on EBSD spatial resolution, Ultramicroscopy. 111 (2011) 1488–1494, doi: 10.1016/j.ultramic.2011.06.007.

[5] R.R. Keller, R.H. Geiss, Transmission EBSD from 10nm domains in a scanning electron microscope, J. Microsc. 245 (2012) 245–251, doi: 10.1111/j.1365-2818.2011.03566.x.

[6] G.C. Sneddon, P.W. Trimby, J.M. Cairney, Transmission Kikuchi diffraction in a scanning electron microscope: a review, Mater. Sci. Eng. R Rep. 110 (2016) 1–12, doi: 10.1016/j.mser.2016.10.001.

[7] J.-.J. Fundenberger, E. Bouzy, D. Goran, J. Guyon, A. Morawiec, H. Yuan, Transmission Kikuchi diffraction (TKD) via a horizontally positioned detector, Microsc. Microanal. 21 (2015) 1101–1102, doi: 10.1017/S1431927615006297.

[8] J.J. Fundenberger, E. Bouzy, D. Goran, J. Guyon, H. Yuan, A. Morawiec, Orientation mapping by transmission-SEM with an on-axis detector, Ultramicroscopy 161 (2016) 17–22, doi: 10.1016/j.ultramic.2015.11.002.

[9] H. Yuan, E. Brodu, C. Chen, E. Bouzy, J.-J. Fundenberger, L.S. Toth, On-axis versus off-axis transmission Kikuchi diffraction technique: application to the characterisation of severe plastic deformation-induced ultrafine-grained microstructures, J. Microsc. 267 (2017) 70–80, doi: 10.1111/jmi.12548.

[10] F. Niessen, A. Burrows, A.B.da S. Fanta, A systematic comparison of on-axis and off-axis transmission Kikuchi diffraction, Ultramicroscopy. 186 (2018) 158–170, doi: 10.1016/j.ultramic.2017.12.017.

[11] N.C. Krieger Lassen, K. Conradsen, D. Juul Jensen, Image processing procedures for analysis of electron diffraction patterns, Scanning Microsc. 6 (1992) 115–121.

[12] F. Ram, S. Wright, S. Singh, M.D. Graef, Error analysis of the crystal orientations obtained by the dictionary approach to EBSD indexing, Ultramicroscopy. 181 (2017) 17–26, doi: 10.1016/j.ultramic.2017.04.016.

[13] Y.-.H. Chen, S.U. Park, D. Wei, G. Newstadt, M. Jackson, J.P. Simmons, M. De Graef, A.O. Hero, A dictionary approach to EBSD indexing, Phys. Stat. (2015) http://arxiv.org/abs/1502.07436 (accessed March 5, 2019).

[14] S. Singh, Y. Guo, B. Winiarski, T.L. Burnett, P.J. Withers, M.D. Graef, High resolution low kV EBSD of heavily deformed and nanocrystalline aluminium-based indexing, Sci. Rep. 8 (2018) 1–8, doi: 10.1038/s41598-018-29315-8.

[15] R. Hielscher, F. Bartel, T.B. Britton, Gazing at crystal balls - Electron backscatter diffraction indexing and cross correlation on a sphere, Cond-Mat. (2018) http://arxiv.org/abs/1810.03211 (accessed May 6, 2019).

[16] W.C. Lenthe, S. Singh, M.D. Graef, A spherical harmonic transform approach to the indexing of electron back-scattered diffraction patterns, Ultramicroscopy. 207 (2019) 112841, doi: 10.1016/j.ultramic.2019.112841.

[17] K.Z. Troost, P. van der Sluis, D.J. Gravesteijn, Microscale elastic-strain determination by backscatter kikuchi diffraction in the scanning electron microscope, Appl. Phys. Lett. 62 (1993) 1110–1112, doi: 10.1063/1.108758.

[18] A.J. Wilkinson, Measurement of elastic strains and small lattice rotations using electron back scatter diffraction, Ultramicroscopy. 62 (1996) 237–247, doi: 10.1016/0304-3991(95)00152-2.

[19] A. Wilkinson, A new method for determining small misorientations from EBSD patterns, Scr. Mater. 44 (2001) 2379–2385.

[20] A.J. Wilkinson, G. Meaden, D.J. Dingley, High resolution mapping of strains and rotations using electron backscatter diffraction, Mater. Sci. Technol. 22 (2006) 1271–1278, doi: 10.1179/174328406X130966.

[21] A.J. Wilkinson, G. Meaden, D.J. Dingley, High-resolution elastic strain measurement from electron backscatter diffraction patterns: new levels of sensitivity, Ultramicroscopy. 106 (2006) 307–313, doi: 10.1016/j.ultramic.2005.10.001.

[22] T.B. Britton, C. Maurice, R. Fortunier, J.H. Driver, A.P. Day, G. Meaden, D.J. Dingley, K. Mingard, A.J. Wilkinson, Factors affecting the accuracy of high resolution electron backscatter diffraction when using simulated patterns, Ultramicroscopy. 110 (2010) 1443–1453, doi: 10.1016/j.ultramic.2010.08.001.

[23] T.B. Britton, A.J. Wilkinson, Measurement of residual elastic strain and lattice rotations with high resolution electron backscatter diffraction, Ultramicroscopy. 111 (2011) 1395–1404, doi: 10.1016/j.ultramic.2011.05.007.

[24] T.B. Britton, A.J. Wilkinson, High resolution electron backscatter diffraction measurements of elastic strain variations in the presence of larger lattice rotations, Ultramicroscopy. 114 (2012) 82–95, doi: 10.1016/j.ultramic.2012.01.004.

[25] C. Maurice, J.H. Driver, R. Fortunier, On solving the orientation gradient dependency of high angular resolution EBSD, Ultramicroscopy. 113 (2012) 171–181, doi: 10.1016/j.ultramic.2011.10.013.

[26] A.J. Wilkinson, Assessment of lattice strain, rotation and dislocation content using electron back-scatter diffraction, J. Phys. Conf. Ser. 326 (2011) 012004.

[27] S. Villert, C. Maurice, C. Wyon, R. Fortunier, Accuracy assessment of elastic strain measurement by EBSD, J. Microsc. 233 (2009) 290–301, doi: 10.1111/j.1365-2818.2009.03120.x.

[28] H. Yu, J. Liu, P. Karamched, A.J. Wilkinson, F. Hofmann, Mapping the full lattice strain tensor of a single dislocation by high angular resolution transmission Kikuchi diffraction (HR-TKD), Scr. Mater. 164 (2019) 36–41, doi: 10.1016/j.scriptamat.2018.12.039.

[29] Y.T. Tang, P. Karamched, J. Liu, J.C. Haley, R.C. Reed, A.J. Wilkinson, Grain boundary serration in nickel alloy inconel 600: quantification and mechanisms, Acta Mater. 181 (2019) 352–366, doi: 10.1016/j.actamat.2019.09.037.

[30] E. Brodu, E. Bouzy, J.-J. Fundenberger, Diffraction contrast dependence on sample thickness and incident energy in on-axis transmission Kikuchi diffraction in SEM, Ultramicroscopy. 181 (2017) 123–133, doi: 10.1016/j.ultramic.2017.04.017.

[31] T.J. Hardin, T.J. Ruggles, D.P. Koch, S.R. Niezgoda, D.T. Fullwood, E.R. Homer, Analysis of traction-free assumption in high-resolution EBSD measurements, J. Microsc. 260 (2015) 73–85, doi: 10.1111/jmi.12268.

[32] T. Vermeij, J.P.M. Hoefnagels, A consistent full-field integrated DIC framework for HR-EBSD, Ultramicroscopy. 191 (2018) 44–50, doi: 10.1016/j.ultramic.2018.05.001.

[33] T.J. Ruggles, G.F. Bomarito, R.L. Qiu, J.D. Hochhalter, New levels of high angular resolution EBSD performance via inverse compositional Gauss−newton based digital image correlation, Ultramicroscopy. 195 (2018) 85–92, doi: 10.1016/j.ultramic.2018.08.020.

[34] Q. Shi, S. Roux, F. Latourte, F. Hild, Estimation of elastic strain by integrated image correlation on electron diffraction patterns, Ultramicroscopy. 199 (2019) 16–33, doi: 10.1016/j.ultramic.2019.02.001.

[35] T. Vermeij, M. De Graef, J. Hoefnagels, Demonstrating the potential of accurate absolute cross-grain stress and orientation correlation using electron backscatter diffraction, Scr. Mater. 162 (2019) 266–271, doi: 10.1016/j.scriptamat.2018.11.030.

[36] C. Zhu, K. Kaufmann, K.S. Vecchio, Novel remapping approach for HR-EBSD based on demons registration, Ultramicroscopy. 208 (2020) 112851, doi: 10.1016/j.ultramic.2019.112851.

[37] B. Pan, K. Qian, H. Xie, A. Asundi, Two-dimensional digital image correlation for in-plane displacement and strain measurement: a review, Meas. Sci. Technol. 20 (2009) 062001, doi: 10.1088/0957-0233/20/6/062001.

[38] B. Pan, Digital image correlation for surface deformation measurement: historical developments, recent advances and future goals, Meas. Sci. Technol. 29 (2018) 082001, doi: 10.1088/1361-6501/aac55b.

[39] B. Pan, Y. Wang, L. Tian, Automated initial guess in digital image correlation aided by Fourier−Mellin transform, Opt. Eng. 56 (2017) 0141031 1−7https://doi.org/, doi: 10.1117/1.OE.56.1.014103.

[40] B. Zitová, J. Flusser, Image registration methods: a survey, Image Vis. Comput. 21 (2003) 977–1000, doi: 10.1016/S0262-8856(03)00137-9.

[41] B. Pan, H. Xie, Z. Wang, Equivalence of digital image correlation criteria for pattern matching, Appl. Opt. 49 (2010) 5501–5509, doi: 10.1364/AO.49.005501.

[42] R. Hartley, A. Zisserman, Projective geometry and transformations of 2D, Mult. View Geom. Comput. Vis. (2004), doi: 10.1017/CBO9780511811685.005.

[43] S. Baker, I. Matthews, Lucas-Kanade 20 years on: a unifying framework, Int. J. Comput. Vis. 56 (2004) 221–255, doi: 10.1023/B:VISI.0000011205.11775.fd.

[44] B.D. Lucas, T. Kanade, An iterative image registration technique with an application to stereo vision, in: Proceedings of the Seventh International Joint Conference on Artificial Intelligence IJCAI, 1981, pp. 674–679.

[45] K. Mingard, A. Day, C. Maurice, P. Quested, Towards high accuracy calibration of electron backscatter diffraction systems, Ultramicroscopy. 111 (2011) 320–329, doi: 10.1016/j.ultramic.2011.01.012.

[46] B. Pan, Reliability-guided digital image correlation for image deformation measurement, Appl. Opt. 48 (2009) 1535–1542, doi: 10.1364/AO.48.001535.

[47] B. Pan, Y. Wang, L. Tian, Automated initial guess in digital image correlation aided by Fourier−Mellin transform, Opt. Eng. 56 (2017) 0141031 1−7https://doi.org/, doi: 10.1117/1.OE.56.1.014103.

[48] E. Brodu, E. Bouzy, J.-J. Fundenberger, J. Guyon, A. Guitton, Y. Zhang, On-axis tkd for orientation mapping of nanocrystalline materials in SEM, Mater. Charact. 130 (2017) 92–96, doi: 10.1016/j.matchar.2017.05.036.

[49] T.B. Britton, D. Goran, V.S. Tong, Space rocks and optimising scanning electron channelling contrast, Mater. Charact. 142 (2018) 422–431, doi: 10.1016/j.matchar.2018.06.001.

[50] T. Ickler, H. Meckbach, F. Zeismann, A. Brückner-Foit, Assessing the influence of crystallographic orientation, stress and local deformation on magnetic domains using electron backscatter diffraction and forescatter electron imaging, Ultramicroscopy. 198 (2019) 33–42, doi: 10.1016/j.ultramic.2018.12.012.

[51] N.C. Krieger Lassen, J.B. Bildesorensen, Calibration of an electron back-scattering pattern set-up, J. Microsc. 170 (1993) 125–129.

[52] T. Tanaka, A.J. Wilkinson, Pattern matching analysis of electron backscatter diffraction patterns for pattern centre, crystal orientation and absolute elastic strain determination − accuracy and precision assessment, Ultramicroscopy. 202 (2019) 87–99, doi: 10.1016/j.ultramic.2019.04.006.

[53] B. Beausir, J.-J. Fundengerger, Analysis tools for electron and X-ray diffraction, atex - software, université de lorraine, Metz (2017) www.atex-software.eu .

[54] J. Blaber, B. Adair, A. Antoniou, Ncorr: open-Source 2D digital image correlation matlab software, Exp. Mech. 55 (2015) 1105–1122, doi: 10.1007/s11340-015-0009-1.

[55] B. Pan, K. Li, W. Tong, Fast, robust and accurate digital image correlation calculation without redundant computations, Exp. Mech. 53 (2013) 1277–1289, doi: 10.1007/s11340-013-9717-6.

[56] B. Pan, An evaluation of convergence criteria for digital image correlation using inverse compositional Gauss−Newton algorithm, Strain 50 (2014) 48–56, doi: 10.1111/str.12066.

[57] N.C. Admal, G. Po, J. Marian, A unified framework for polycrystal plasticity with grain boundary evolution, Int. J. Plast. 106 (2018) 1–30, doi: 10.1016/j.ijplas.2018.01.014.

[58] S. Sun, B.L. Adams, W.E. King, Observations of lattice curvature near the interface of a deformed aluminium bicrystal, Philos. Mag. A. 80 (2000) 9–25, doi: 10.1080/01418610008212038.

[59] B.S. El-Dasher, B.L. Adams, A.D. Rollett, Viewpoint: experimental recovery of geometrically necessary dislocation density in polycrystals, Scr. Mater. 48 (2003) 141–145, doi: 10.1016/S1359-6462(02)00340-8.

[60] W. Pantleon, Resolving the geometrically necessary dislocation content by conventional electron backscattering diffraction, Scr. Mater. 58 (2008) 994–997, doi: 10.1016/j.scriptamat.2008.01.050.

[61] A.J. Wilkinson, D. Randman, Determination of elastic strain fields and geometrically necessary dislocation distributions near nanoindents using electron back scatter diffraction, Philos. Mag. 90 (2010) 1159–1177, doi: 10.1080/14786430903304145.

[62] J. Jiang, T.B. Britton, A.J. Wilkinson, The orientation and strain dependence of dislocation structure evolution in monotonically deformed polycrystalline copper, Int. J. Plast. 69 (2015) 102–117, doi: 10.1016/j.ijplas.2015.02.005.

[63] Prior, Problems in determining the misorientation axes, for small angular misorientations, using electron backscatter diffraction in the sem, J. Microsc. 195 (1999) 217–225.

[64] L. Zhang, T. Wang, Z. Jiang, Q. Kemao, Y. Liu, Z. Liu, L. Tang, S. Dong, High accuracy digital image correlation powered by GPU-based parallel computing, Opt. Lasers Eng. 69 (2015) 7–12, doi: 10.1016/j.optlaseng.2015.01.012.

[65] Y. Su, Q. Zhang, Z. Fang, Y. Wang, Y. Liu, S. Wu, Elimination of systematic error in digital image correlation caused by intensity interpolation by introducing position randomness to subset points, Opt. Lasers Eng. 114 (2019) 60–75, doi: 10.1016/j.optlaseng.2018.10.012.

[66] J. Sánchez, The inverse compositional algorithm for parametric registration, Image Process. Line. 6 (2016) 212–232, doi: 10.5201/ipol.2016.153.

[67] S. Derrode, F. Ghorbel, Robust and efficient fourier−mellin transform approximations for gray-level image reconstruction and complete invariant description, Comput. Vis. Image Underst. 83 (2001) 57–78, doi: 10.1006/cviu.2001.0922.

[68] Q.-S. Chen, M. Defrise, F. Deconinck, Symmetric phase-only matched filtering of Fourier−Mellin transforms for image registration and recognition, IEEE Trans. Pattern Anal. Mach. Intell. 16 (1994) 1156–1168, doi: 10.1109/34.387491.

[69] B.S. Reddy, B.N. Chatterji, An FFT-based technique for translation, rotation, and scale-invariant image registration, IEEE Trans. Image Process. Publ. IEEE Signal Process. Soc. 5 (1996) 1266–1271, doi: 10.1109/83.506761.

[70] P.R. Smith, Bilinear interpolation of digital images, Ultramicroscopy. 6 (1981) 201–204, doi: 10.1016/S0304-3991(81)80199-4.

[71] A. Foden, D.M. Collins, A.J. Wilkinson, T.B. Britton, Indexing electron backscatter diffraction patterns with a refined template matching approach, Ultramicroscopy. 207 (2019) 112845, doi: 10.1016/j.ultramic.2019.112845.